2010

Automated Measurement of Midline Shift in Brain CT Images and its Application in Computer-Aided Medical Decision Making

Chen Wenan
Virginia Commonwealth University

School of Engineering

Virginia Commonwealth University

This is to certify that the dissertation prepared by Wenan Chen entitled AUTOMATED MEASUREMENT OF MIDLINE SHIFT IN BRAIN CT IMAGES AND ITS APPLICATION IN COMPUTER-AIDED MEDICAL DECISION MAKING has been approved by his committee as satisfactory completion of the Dissertation requirement for the degree of Doctor of Philosophy

---

Kayvan Najarian, Ph.D., Committee Chair, Department of Computer Science

---

Krzysztof Cios, Ph.D., Chair of Computer Science, School of Engineering

---

Vojislav Kecman, Ph.D., Dept. of Computer Science, School of Engineering

---

Rosalyn S. Hobson, Ph.D., School of Engineering

Toan Huynh, M.D., Carolinas Health System

Kevin R. Ward, M.D., School of Medicine

Rosalyn S. Hobson, Associate Dean of Graduate Studies, School of Engineering

---

Russell D. Jamison, Ph.D., Dean, School of Engineering

F. Douglas Boudinot, Ph.D., Dean of the School of Graduate Studies

---

Date

AUTOMATED MEASUREMENT OF MIDLINE SHIFT IN BRAIN CT IMAGES AND ITS APPLICATION IN COMPUTER-AIDED MEDICAL DECISION MAKING

A dissertation submitted in partial fulfillment of the requirements for the degree of Doctor of Philosophy at Virginia Commonwealth University.

by

WENAN CHEN
B.S., Beijing Information Technology Institute, 2003
M.S., Beijing University of Technology, 2006

Director: KAYVAN NAJARIAN
ASSOCIATE PROFESSOR, DEPARTMENT OF COMPUTER SCIENCE

Virginia Commonwealth University
Richmond, Virginia
March, 2010

Acknowledgments

This dissertation could not have been written without Kayvan Najarian who not only served as my advisor but also encouraged and challenged me throughout my academic program. I am very much impressed and influenced by his way of research and life, which include general methods in research, extensive knowledge and ideas in research, optimistic attitude when facing problems, dedication to the objectives, humor in life and the way of enjoying life. These will definitely help me significantly in my future career. I would like to give sincere gratitude to Kayvan for all his great help and support both on my research on personal life.

I also would like to give my thanks to Dr. Krzysztof Cios, Dr. Vojislav Kecman, Dr. Rosalyn S. Hobson, Dr. Toan Huynh and Dr. Kevin R. Ward. All questions and suggestions from my committee members helped me to improve the quality of the research.

My thanks also go to all my colleagues in the lab, they are: Dr. Soo-Yeon Ji, Dr. Simina Vasilache, Dr. Rebecca (Alex) Smith, NaZanin Mirshahi, Egle Verdingovaite, Sumeyra Demir, Yurong Luo, Kevin Akselrod, Abed Al Raoof Bsoul, Sardar Ansari, Ashwin Belle, Sharad Shandilya. You guys brought the lab plenty of fun as well as small disputes which helped to understand each other better:). As a group together, we have collaborated, helped and learned a lot from each other.

Last but not least, I would like to give my special thanks to my family, especially my mother Fengxian Chen. She has inspired me all the way and set my goal even when I was

a child. If obtaining the PhD degree is an achievement, at least half of the achievement is attributed to her. I also would like to thank my wife Yan Li. Without her love and care, the road of life would not be so happy and smooth.

Table of Contents

Page

List of Tables

List of Figures

Abstract

AUTOMATED MEASUREMENT OF MIDLINE SHIFT IN BRAIN CT IMAGES AND ITS APPLICATION IN COMPUTER-AIDED MEDICAL DECISION MAKING

By Wenan Chen, Ph.D.

A dissertation submitted in partial fulfillment of the requirements for the degree of Doctor of Philosophy at Virginia Commonwealth University.

Virginia Commonwealth University, 2010

Major Director: Kayvan Najarian
Associate Professor, Department of Computer Science

The severity of traumatic brain injury (TBI) is known to be characterized by the shift of the middle line in brain as the ventricular system often changes in size and position, depending on the location of the original injury. In this thesis, the focus is given to processing of the CT (Computer Tomography) brain images to automatically calculate midline shift in pathological cases and use it to predict Intracranial Pressure (ICP). The midline shift measurement can be divided into three steps. First the ideal midline of the brain, i.e., the midline before injury, is found via a hierarchical search based on skull symmetry and tissue features. Second, the ventricular system is segmented from the brain CT slices. Third, the actual midline is estimated from the deformed ventricles by shape matching method. The horizontal shift in the ventricles is then calculated based on the ideal midline and the

actual midline in TBI CT images. The proposed method presents accurate detection of the ideal midline using anatomical features in the skull, accurate segmentation of ventricles for actual midline estimation using the information of anatomical features with a spatial template derived from a magnetic resonance imaging (MRI) scan, and an accurate estimation of the actual midline based on the robust proposed multiple regions shape matching algorithm. After the midline shift is successively measured, features including midline shift, texture information of CT images, as well as other demographic information are used to predict ICP. Machine learning algorithms are used to model the relation between the ICP and the extracted features. By using systematic feature selection and parameter selection of the learning model, promising results on ICP prediction are achieved. The prediction results also indicate the reliability of the proposed midline shift estimation.

Executive Summary and Contributions

Traumatic brain injury (TBI) is both a very severe and common injury in the United States. The major complication of TBI is increased intracranial pressure (ICP), which can prove fatal. Measuring ICP level is therefore very important when treating TBI patients. Since high ICP causes deformation of brain tissue, this deformation can be used to estimate ICP. A typical representation of brain tissue deformation is the amount of midline shift in the brain. In this thesis, a framework for automated midline shift measurement is proposed, including:

- A hierarchical method to accurately extract the ideal midline from CT images according to the exact anatomical features routinely used by physicians. This is explained in more detail in Chapter 3.

- A hierarchical method to accurately segment the ventricular system from CT images. This is explained in more detail in Chapters 4 and 5.

- A hierarchical method to accurately estimate the actual midline based on segmentation of the ventricular system with the proposed multiple regions shape matching algorithm. Details are provided in Chapter 6.

- A machine learning based method to predict ICP based on features extracted from both CT images and other information such as demographics. Details can be found at the end of Chapter 7.

Automated analysis of brain CT using image processing can result in higher accuracy, as many features that visual inspection can easily miss would be detected using digital image processing. The proposed system will also offer benefits of consistency and wide availability; it can be used for hospitals in rural areas as well as for the military to help care givers make more informative decisions. The method's low cost and fast speed will save physicians time by creating recommendations faster, without proving impractical to implement.

The impact in other fields of image processing is as follows. Generally, other medical imaging modality than CT imaging can apply the proposed methods to perform segmentation, feature points based alignment and automated measurement from labeled templates. The developed methods can be directly applied to the following applications: segmentation of pelvic CT images; segmentation of brain MRI, abdominal MRI and pelvic MRI.

CHAPTER 1 Introduction

It is estimated that every year, 1.4 million people in the United States sustain a traumatic brain injury(TBI) [36]. TBI occurs when a sudden event damages the brain, such as a blow or jolt to the head. Over 50,000 of these patients will not survive, and many others will be left permanently disabled [36]. 50% of those who die do so within the first two hours after injury [65]. Speed of diagnosis is therefore vital, and so Computed Tomography (CT) imaging, which is faster and much less costly than other medical scans, e.g., MRI scan, is still the gold standard for initial TBI assessment [63]. A CT scan can also clearly reveal any severe abnormalities such as fractures or hematomas. Figure 1.1 shows a brain MR image set and an axial CT slice image. One common cause of death and other serious long-term complications after TBI is increased intracranial pressure (ICP) resulting from edema caused by the original injury. Increased ICP causes shift and deformation of brain tissue, complicating the injury further and rapidly proving fatal if unchecked. Cranial trepanation allows a monitoring device to be placed inside the skull, but puts the patient at risk of infection, bleeding, and further damage to the brain tissue. If possible, a non-invasive pre-screening method to evaluate the need for cranial trepanation is preferable. A CT scan is usually taken soon after TBI in emergency setting. It may show shifting of the tissue - "midline shift" - or a significant change in the size of the lateral ventricles. The shift and size of ventricles can either suggest for or against performing

cranial trepanation. Physicians may use both these features to evaluate the severity of the ICP, but these calculations have to be done manually and are time consuming. Moreover, these estimations cannot incorporate details that are not perceivable by visual inspection, such as detailed variations in CT scan. In order to improve accuracy, speed and consistency, automated processing of this procedure is preferred. This work proposes a method to automate the calculation of the midline shift from a CT scan, including method of detecting the ideal midline (where "ideal" refers to the position expected in a normal non-pathological subject), segmenting the lateral and third ventricles, and estimating the actual midline position.

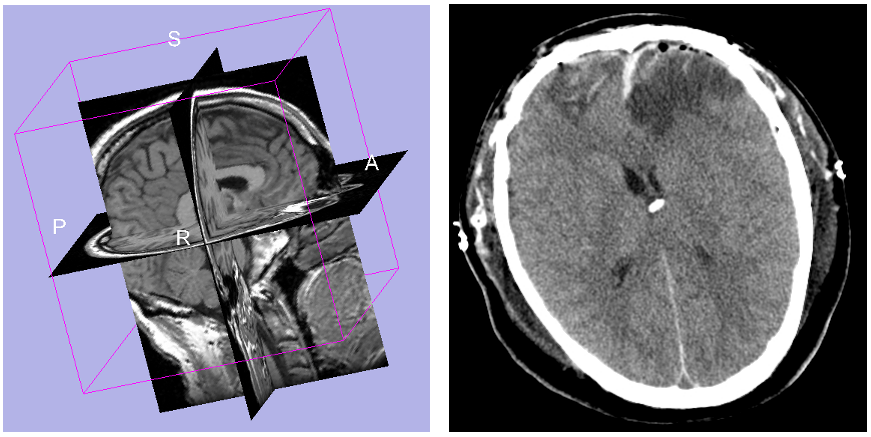

(a) 3D MR images of brain from 3D slicer sample visualization

(b) One axial CT slice

Figure 1.1: MR and CT Images of brain.

In a clinical setting, usually the septum pellucidum (SP), pineal gland (PG), or third ventricle are chosen as reference points for measurement of the midline shift. Figure 1.2 shows the anatomy structure of SP and PG in MR images. In a normal brain, these anatomy structures should be in the middle plane separating left and right hemispheric

brains. This means that there is no shift in midline. In pathological cases, such as tumor or hematomas, unbalanced pressure may exist and push one side of the brain to the other side. The direct result is the location change or shift of these structures. The shift is typically measured in two ways. One is to measure the difference in distance between the reference point and each side of the skull [91], see Figure 1.3. The other is to measure the distance between the reference point and a imaginary line, called the ideal midline, which divides the brain into two nearly symmetric halves [89], see Figure 1.4[1]. In [89], PG and SP are used as reference points and the vertical line connecting the anterior and posterior insertions of falx cerebri is used as the ideal midline. The midline shift is used as one prognostic factor to predict postoperative restoration of consciousness in patients with chronic subdural hematomas.

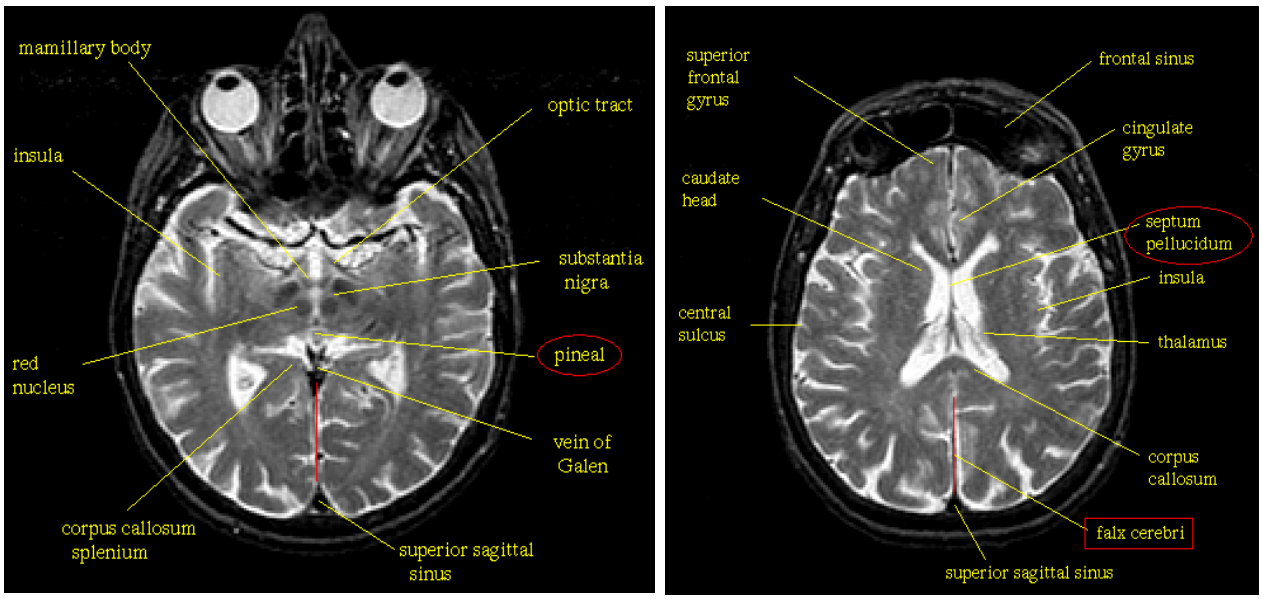

Figure 1.2: SP and PG location from the Whole Brain Atlas.

[1]Image from CT scan guidance, http://www.crash.lshtm.ac.uk/

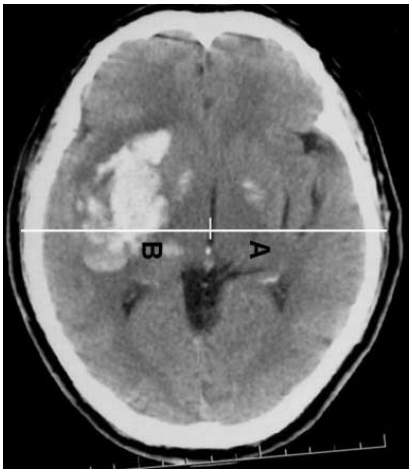

Figure 1.3: Midline shift measured using third ventricle and the difference in distance from each side of skull, image from [91].

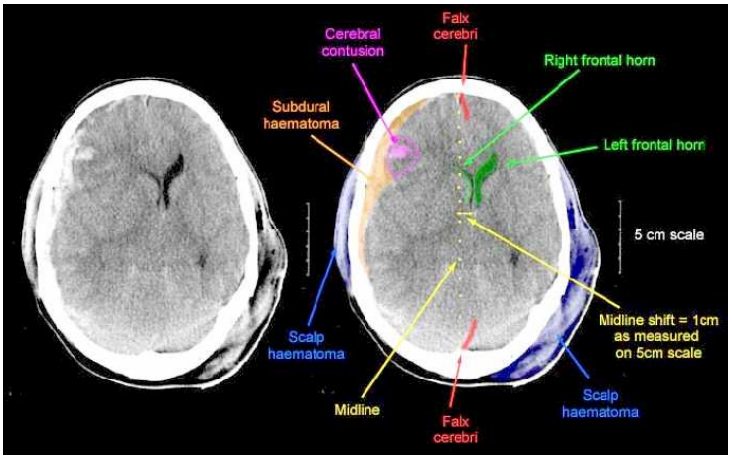

Figure 1.4: Midline shift measured using lateral ventricle and falx cerebri.

Because SP and PG are relatively small and not obvious in CT images, in this study, it was decided to use ventricles to define the reference point. The ventricular system is a set of structures filled with cerebrospinal fluid (CSF) and typically visible in CT scans. Figure 1.5 shows a 3D model of ventricular system with the presence of a MR slice of the brain. It deforms when the pressure is changed inside the brain. Therefore it is a very suitable candidate structure to measure the deformation of brain tissue in pathological cases. In this study, it is proposed to automatically measure the midline shift through detecting the deformation of the ventricular system, including lateral ventricles, the third ventricle[2] in brain CT images. Since in this study the entire ventricular system (except the fourth ventricle) is used to measure the midline shift in brain rather than one or two reference points, it should provide more information about the brain tissue deformation and corresponding injury details. In this research, it is assumed that the CT scan images are axial slices of the brain. This is usually the case when CT scan is taken.

In order to automate the entire measurement process, it is imperative to automate the ideal midline detection for each slice, which serves as the reference line. Then ventricular systems need to be segmented to define reference points. Based on the segmented ventricular system, a series of reference points or lines representing the new locations of the actual midline can be estimated. Figure 1.6 shows the flow chart of the whole process. After the midline shift is measured, this feature is used to predict related outcome. Figure 1.7 illustrates the estimation of midline shift for different CT slices based on the proposed framework. One possible application is the ICP prediction. By combining features such as midline shift, the brain tissue texture from CT images and other demographic information,

[2]The fourth ventricle is not considered in this work because it is rarely used to measure the midline shift, but it can be easily included.

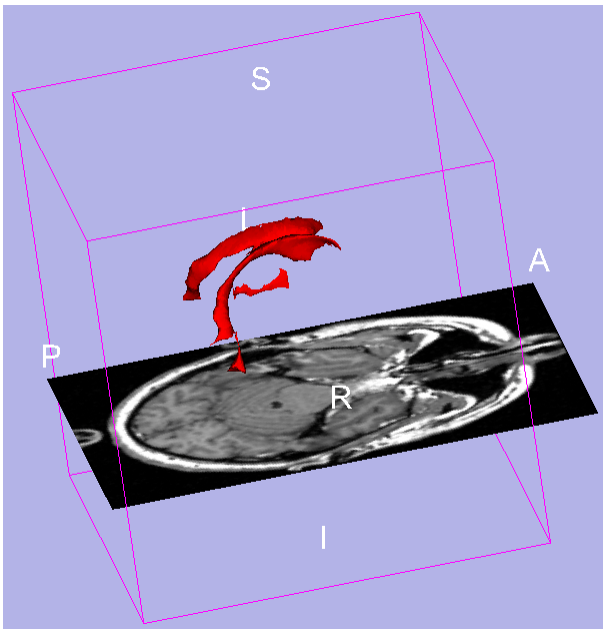

Figure 1.5: 3D ventricle model from 3D slicer sample visualization.

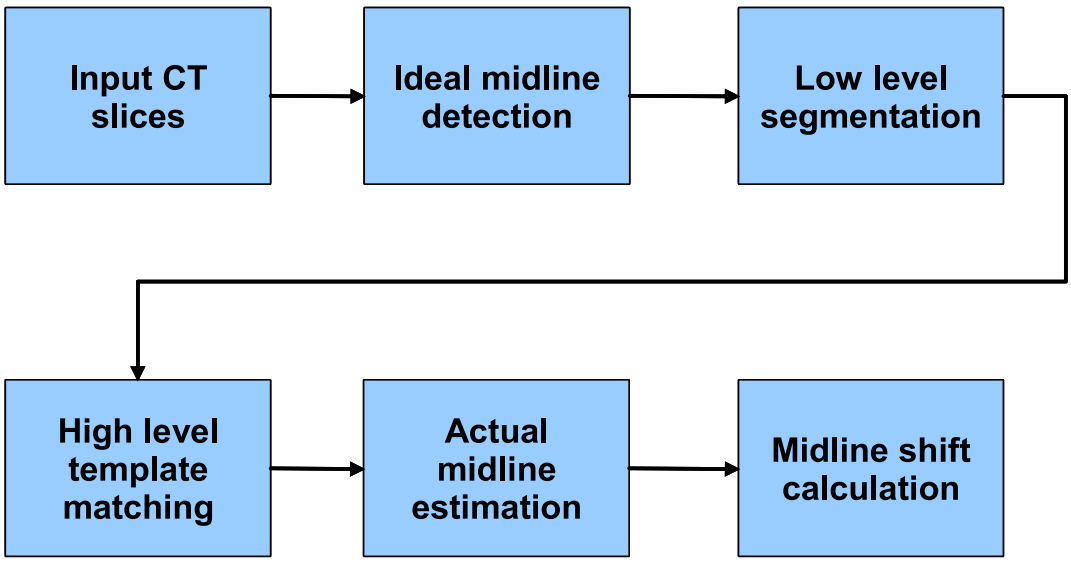

Figure 1.6: The framework of midline shift calculation.

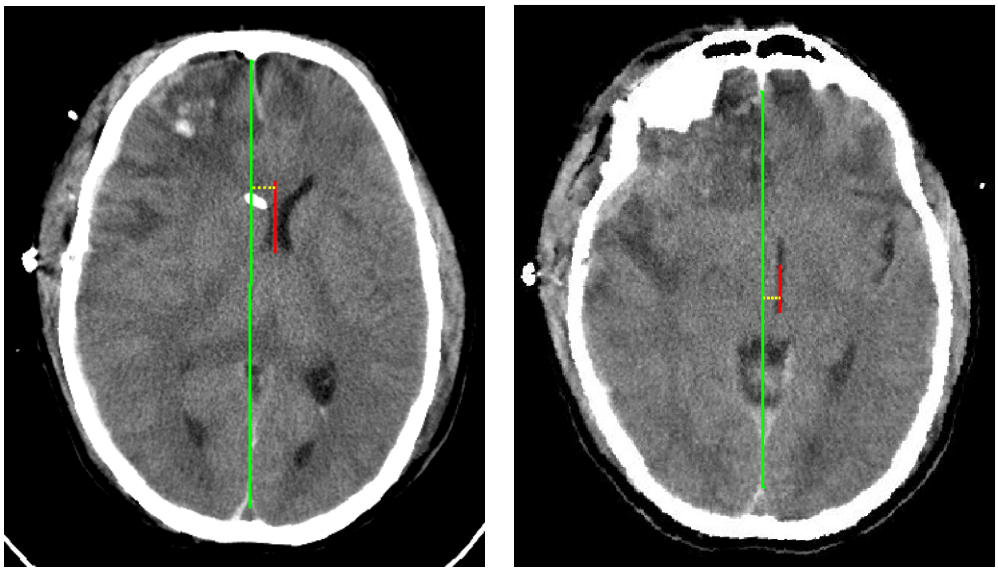

(a) (b)

Figure 1.7: Midline shift calculation based on different CT slices. Figure7(a) shows the calculation based on bilateral ventricles. Figure7(b) shows the calculation based on the third ventricle.

a classifier can be trained to predict the ICP outcome.

In sum, the proposed research encompasses the following components:

- An automated method to accurately extract ideal midline from CT images according to the anatomy feature used by physicians.
- An automated method to accurately segment ventricular system from CT images
- An automated method to accurately estimate the actual midline based on segmentation of ventricular system with the proposed multiple regions shape matching
- An automated machine learning based method to predict ICP based on features extracted both from images and other sources.

The rest of this thesis is organized as follows. Chapter 2 gives a review of biomedical images processing methods. Proposed methods and experiment results are presented in Chapters 3, 4, 5, 6 and 7. Chapter 3 explains the method of ideal midline detection. Chapters 4 and 5 explain the segmentation of ventricular system in CT images. In Chapter 6, a shape matching based actual midline estimation is presented. Chapter 7 applies the extracted features from CT images as well as features from other sources to predict Intracranial Pressure (ICP) level of patients having traumatic brain injury (TBI). Chapter 8 concludes the thesis and lists potential future work.

CHAPTER 2 Previous Studies on Medical Images Processing

2.1 Midline Estimation

In general, the midline refers to the inter-hemispheric sagittal plane which separates the left and right hemispheres [90]. If the brain is healthy (without any traumatic injury), the midline should not change its location inside brain. However, in pathological cases, e.g., in presence of tumors or hematomas, the midline may deform and shift away from its original location. In this work the ideal midline refers to the original midline before any pathological change. The actual midline refers to the actual current position of the midline in brain. Sometimes the ideal midline, or ideal mid-sagittal plane, is defined differently. In [78] [103], ideal mid-sagittal midline is defined as the plane that maximizes the symmetry of the brain. Others define the midline based on the physical structure of the brain: the plane that best represents inter-hemispheric fissure. This is closer to the actual midline definition as used in this study. However, all these definitions are very close in practice. The specific definitions used in this study is indeed what is used in a radiologist's measurement of midline shift. These definitions are the result of discussion with radiologists. As such other ideal midline definitions will be referred to as virtual midline. As far as we know, this work is the first research trying to automate the ideal midline detection and the actual midline estimation in CT images based on the physical definition given above. Other research work on medical image processing try to define a symmetric based measurement as the midline, which can be used as a starting point to

further exact ideal midline, for example, [103] [78]. There are also research on medical image segmentation [41] [47, 66, 96] [20] [56] [46], and shape matching applied on medical images [94] [64]. However, this work is the first time trying to automate the midline shift measurement.

2.1.1 The Ideal Midline/Mid-sagittal Plane Estimation

As explained above, methods for automated virtual midline detection can be grouped into two major approaches: inter-hemispheric fissure based [59] [9] and symmetry criterion based methods [78]. These midlines can be used as an approximate location of the ideal midline as defined in this study. In [78] and [103], the mid-sagittal plane is defined based on a plane that divides the 3D brain structure using maximal symmetry. These methods can effectively deal with some asymmetry by using either a robust registration method or an estimation method, as shown in experiments. The advantage of this symmetry based method is that it is robust to the local asymmetry due to pathological changes. The disadvantage is that this method often lacks anatomical accuracy, even though usually it is very close to inter-hemispheric fissure. The fissure based method [58] [9] approximates the virtual midline based on the points representing the fissure. The disadvantages of this method include its needs to accurate detection of the fissure and sensitivity to outliers. Another drawback is that the curvature of the fissure may not be well represented based on the plane. The method proposed here is essentially a combination of these two approaches that results accurate detection of the ideal midline. In the proposed approach bone symmetry is used to form an approximate midline, then anatomical features in CT images are used to direct and improve the approximate midline to capture the ideal midline. Because the final aim is to measure the midline shift, using symmetric measures

alone cannot guarantee that the result is consistent with the actual location of an ideal fissure, (i.e. the fissure before TBI), which may not precisely define the plane separating the two sides symmetrically.

2.1.2 The Actual Midline Estimation

The fissure based midline detection can also be viewed as an actual midline estimation method. Usually these methods uses deformable model, e.g., snakes that capture the fissure [58]. However, this type of detection method is used in MR images where the fissure is more obvious than CT images. The actual midline in CT images is best represented by the falx cerebri and ventricle locations. For example, in the center axial CT slices where ventricles reside, falx cerebri is only visible at the edges of the anterior and posterior regions. In [54], a genetic algorithm is applied to model the deformed midline using Bézier curve. This method, however, assumes symmetric textures in the brain tissue, which is clearly not always the case especially when hematomas or other pathological changes occur. Also, the method may not work accurately when the midline shift is larger than 5 mm, which reflects the asymmetry present in most pathological cases.

2.2 Medical Image Segmentation Methods

Image segmentation involves assigning a label to each pixel to group them together, based on some common features depending on the objective of the application. Typically the each segmented region may not be directly related to a single meaningful object, e.g., they may only represent one part of a complex object. However segmentation is typically the first step in image processing.

Medical images, e.g., CT scans or MRI scans, have several special characteristics dif-

ferent from general images. These characteristics include:

- Meaningful intensity values. The intensity value corresponds to X-ray attenuation or magnetic resonance frequency of the tissue represented by the pixel (voxel). This is different from natural scene images which have multiple intensity values for the same material under different illumination.

- Solid representations of fixed structure inside the brain. Generally, the brain is a closed space and all objects inside have their approximate positions. The size and position information for each object are roughly known. This information is often approximately represented by brain atlases formed from CT and MRI collections . Although there are differences between individuals, the general structure of these objects is more or less the same.

- Inclusion of a large number of objects. This makes brain segmentation a challenging task, in particular if the aim is to segment the regions representing all different tissue. This is further complicated by the low resolution of the images. Usually segmentation methods for CT scans merge a number of similar parts into larger classes of regions to reduce the overall number of segmented objects.

- Inclusion of blurred boundaries. This is due to partial volume effect which averages the intensity value of neighboring tissues. No segmentation method should be expected to segment regions with accuracies beyond the limits of the image resolution provided to the algorithm.

- Variations due to pathological cases. This increases the difficulty of segmentation

because there can be severe changes inside the brain. A successful segmentation algorithm must be robust enough to deal with these variations.

A medical image segmentation method should utilize/consider these features to gain suitable performance. In medical image segmentation literature, several automated segmentation techniques have been extensively studied for medical images, in particular method for segmentation of MRI scans [76]. In this section, typical medical image segmentation methods are grouped into larger categories and are reviewed. The categories are based on the main feature of the methods and may not be mutually exclusive. A practical image segmentation method belongs to more than one category because it uses more than one feature.

2.2.1 Thresholding

Thresholding methods typically use an intensity threshold to separate foreground objects from background objects. There are global thresholding and local thresholding approaches [27]. Global thresholding method finds a global threshold for each pixel. A popular approach to automatically pick up the threshold is Otsu method [69], which can be viewed as a two-category clustering method using only intensity feature. Local thresholding considers the change of intensities in different area of the image and estimate local thresholds for different areas of an image [27]. The advantages of thresholding method include simplicity, intuitiveness and speed. The limitation of thresholding method is that it only uses intensity information for segmentation. This makes the method fail in highly noisy images. In medical image segmentation, thresholding can be used to segment high contrast regions, e.g., to segment bones form brain tissue in CT images. It also is used for

an initial segmentation.

2.2.2 Region Growing

Region growing uses some initial point as seeds and grow these seeds according to predefined criteria. Seeds can be chosen manually or automatically according to images features. The criteria used for region growing depend on specific applications. Usually edge information, intensity or gradient information is used in the criteria. Several rules can be used to define the criteria, therefore region growing is in fact a general framework to incorporate other information in the algorithm. Region split-and-merge [27] is an algorithm related to region growing which does not require seed points. The advantage of region growing method is that it is natural and intuitive. However, the success of region growing depends heavily on the chosen criteria. Usually the method of choosing criteria is heuristic. Region growing is commonly used in 3D image scan because it allows segmentation across 3D space [85] [83].

2.2.3 Clustering and Classifiers

Since the objective of segmentation is to label each pixel, it is intrinsically a classification or clustering problem. More specifically, the sample information is not only expressed by its intensity value, but also by the neighborhood information. There are three common used clustering methods: K-means [24], Fussy c-means (FCM) [8] and expectation-maximization (EM) [98]. K-means first chooses the number of clusters and initial centroid of each cluster from data points. Then it iteratively clusters data points to its closest centroid and calculate the new centroids based on formed cluster. The algorithm continues until there is no change in the membership of clusters. FCM allows one point to

have membership to more than one cluster and uses possibility value between 0 and 1 to describe these memberships. After the algorithm converges, it picks the cluster with the largest membership value as the pixel label. In [31], FCM clustering method is combined with bias field modeling for MRI segmentation. FCM is also modified in [75] to compensate for inhomogeneities in MRI. EM method is widely used as a method to estimate both missing data and model parameters [19]. In image segmentation, it is usually coupled with Gaussian Mixture Model (GMM). GMM is a commonly used model in classification [48] [10] [29]. GMM models the distribution of samples with a weighted multiple Gaussian function:

$$f(x;\pi,\theta) = \sum_{i=1} K\pi_i f_i(x;\theta_i) \tag{1}$$

After the estimation of GMM parameter, Bayes decision rule can be applied to classify each pixel. In order to decide the parameters in Equation 1, a popular approach is to use some labeled sample data, i.e., labeled pixels to estimated Gaussian distribution parameters. Another method is to first use clustering method, e.g., K-means, to obtain an initial segmentation. Parameters then are estimated based on the initial segmentation result. If the aim is to maximize the likelihood of the model with the data, EM method is typically used to iteratively update model parameters until a local maximal achieved. In [98], GMM is used to model the intensity in MRI. This approach also incorporates another variable for each pixel to model the inhomogeneity. In [29], each brain regions is modeled using GMM and a specific initialization method designed for GMM. Pixel location is also used as a feature in the model. Other classifiers, such as artificial neural networks, are also explored for segmentation of multi-spectral MRI scans [80]. The main advantage of K-means and FCM is their speed and relatively reasonable segmentation

accuracy. However, in many applications using K-means, FCM or EM only focus on pixel intensity. This results in wrong segmentation in particular in presence of noise. Classifier based segmentation methods usually include two main steps: model design and model parameter estimation. Often EM based parameter estimation is very sensitive to initialization.

2.2.4 Markov Random Field Models

Markov Random Field (MRF) assumes that the image label is a realization of Markov Random Field. For each pixel label x_i on location i, denote N_i the neighborhood of the pixel i, then MRF defines the following probabilistic model:

$$p(x_i|x_j, all\ j \neq i) = p(x_i|x_j, j \in N_i) \tag{2}$$

The main idea of MRF model is that the label in one location depends on its neighboring pixels. This has two consequences. First the labels of local neighborhood cannot change arbitrarily as it must satisfy some probability distribution described in Equation 2. Second, the constraint is not global, only local influence is imposed by one label. This constraint enables MRF model to easily adapt to image data while maintaining smooth segmentation. There are several methods to maximize the probability of label configuration given the image data under the MRF model. One is simulated annealing (SA) [26], which guarantees maximal convergence given infinite training time. SA is very computationally extensive. Another method is Iterated Conditional Modes (ICM) [6], which is equivalent to instantaneous freezing in simulated annealing. Other methods are also proposed including mean field (MF) methods [25]. Typically MRF assumes Gaussian distribution when modeling the intensity value with each label. Besag [6] uses ICM method for image restoration from

noisy data. The experiment in [6] can be thought of as image segmentation because the final results are regions with several different levels. Papas [71] applies the MRF model but allows different mean estimation in local areas of the same class. This local adaptive consideration performs much better than the simple K-means algorithm using global criteria for all pixels. In [53], multi-spectral MRI segmentation is achieved using GMM to model image intensity and MRF model a priori. Held [33] uses two MRF models to conduct MR image segmentation; one for the inhomogeneous gain field and one for the MRF prior. In [79], a very similar method to [71] is applied, except that it allows different variances for different locations in Gaussian distribution in the same class. Recent studies involve Hidden MRF [105] and compound MRF [99]. The main advantage of the MRF model is that it models the spatial relation which is very common in natural images. Usually this achieves smoothers segmentation than other intensity based segmentation methods. However, the MRF method is often computationally intensive, especially while SA algorithm is used. Another disadvantage of the MRF model is its needs for careful initialization.

2.2.5 Deformable Models

Deformable models use a parameterized curve, surface, or even solid model to fit image data. The initial model deforms under the influence of internal and external forces. Internal forces are computed from within the model to keep it smooth throughout the deformation. External forces are usually derived from the image to drive the curve, surface or solid model to fit the data. A popular family of deformable models is "snake" [40]. This model is used in many medical applications [5] [55] [18]. Another deformable model, based on statistical templates, is active shape model [17]. It applies manually labeled points to learn the statistical features of the shape and guides the model to deform the contour in

the direction that may leads to a better fit. There are also other deformable models [61]. The advantages of deformable models include their ability to directly generate closed parametric curves, surfaces, solid models from image data. The model usually has smoothness constraint, and as such the result is robust even in noisy cases. A disadvantage of most deformable model is their need for manual interaction or initialization with points close to the border of the structure to be segmented. Besides, the model parameters need to be chosen appropriately. Research aiming to reduce the sensitivity of initialization and to enhance the ability of modeling complex shapes shows promising results in [60] [102].

2.2.6 Knowledge Driven Methods

One difference between computer based segmentation and visual segmentation done by human is that a human uses substantial amount of domain knowledge throughout the process. Incorporating human-level prior knowledge into computer algorithms greatly enhances the ability of computers in solving various problems in which human outperforms the machine, such as vision and visual recognition. One popular approach incorporating prior knowledge in medical image segmentation is the use of a medical atlas [92, 77]. The common use of an atlas is to register the atlas images with the target images [57]. Once the registration is done, the target image is segmented according to the know structure of the atlas. Since registration emphasizes global alignment between the two images, detailed differences between the atlas and the target image may not be well addressed. As discussed above, region growing is also a method of incorporating prior knowledge. First region growing embodies the continuity of the objects in images by growing connected neighborhood. In 3D MRI data, adjacent slices may be checked for growing criteria. Xia et al. [100] applies region growing to extract ventricles in the brain from MRI scans, designing

very specific rules to grow each part into the entire ventricular system. Li [52] designs a Generic Blackboard (GBB) based system to organize tissue location information. GBB is a basis for the construction of problem-solving systems including reasoning and data representation. Together with low level image features such as points, lines, and regions, this system is intuitive and shows relatively suitable delineation results for different tissue regions. In [85], cognition network technology is used to control ventricle detection. This method is convenient to set constraints in a high level form which facilitates the use of expert knowledge. These methods of incorporating expert knowledge are very general and can also be applied to segment or detect other brain objects. Incorporating human knowledge into algorithms mimics human's reasoning process and can implement heuristics formed from the human knowledge.

2.2.7 Conclusion

For particular applications, the above segmentation methods are often combined together to achieve superior performances. For instance, MRF methods are commonly used as a prior to enforce spatial regularization. In [39], expectation maximization based segmentation is combined with the use of active contour models. The more information used in algorithms to characterize each region, the more accurate the segmentation results are. The specific choice of segmentation methods depends on the application field, the image characteristic, and the information to be incorporated throughout the process of segmentation.

CHAPTER 3 Ideal Midline Detection

3.1 Introduction

Increased ICP can cause the actual midline of the brain to move from its original position. The detection of the ideal midline - i.e., the midline that should be present in a healthy brain with normal ICP - serves two purposes. First the ideal midline can be used as a reference line to measure the shift in the brain tissue. Second, it can also be used as a calibration line, as different CT scans have different head rotation depending on the patient's position. Once the CT images are calibrated based on the ideal midline, the entire anatomical structure of the brain can be roughly identified. This provides the opportunity of using a template matching method for ventricle recognition.

3.2 Methods

3.2.1 Overview

The method described in this thesis uses the bone protrusion on the upper part of the skull and the falx cerebri fold in the lower part to accurately locate the position of the ideal midline, since these anatomical features change very little with midline shift in the brain. Although the ideal midline can be roughly approximated using the symmetry of the brain, the anatomical features must be considered for more accurate detection. The ideal midline detection method has three steps:

1. Detect the approximate midline using symmetry.

2. Detect the falx-cerebri and anterior bone protrusion.

3. Use these features to refine the midline position.

Each slice is processed independently at first, then an adjustment is applied across the scan set to compensate for inaccurate midline detection in individual slices.

3.2.2 Detection of Approximate Position of the Ideal Midline Using Symmetry

To find the approximate ideal midline, the algorithm uses an exhaustive rotation angle search around the mass center of the skull to find the line that maximizes the symmetry of the resulting halves. Figure 3.1 outlines this algorithm. First the bone image is extracted using a thresholding method. The image is then rotated around the center of mass of bone parts in the image. Finally, the symmetry of resulting image is measured. Symmetry is defined here as the sum of the symmetry of each row in the resulted image. The row symmetry is defined as the difference in distance between each side of the skull edge and the current approximate midline. Figure 3.2 illustrates the symmetry measurement. For each rotation direction θ_j, the symmetry cost S_j is defined as follows:

$$S_j = \sum_{i=1}^{n} |l_i - r_i|, \tag{3}$$

where n is the number of rows for the skull in the image and measures l_i and r_i are depicted in Figure 3.2. The proposed method resembles the method used in [54], except that in this assessment both the interior edge of skull and the exterior edge of skull is checked. Usually the interior edge is unaffected by the thickness of the skull wall, whereas using the exterior edge may prove problematic if the skull wall is not of uniform thickness. Figure 3.3 demonstrates such a case; the first image is the result of using thickness of skull

bones for symmetry measurement, and the second uses the difference in distance from the searched line to each side. However, in some cases, especially in the lower part of brain, the presence of shape irregularities inside the skull makes the exterior edge a better choice for evaluating symmetry. Consequently, both the interior and exterior edges are tested, and the edge with better symmetric measurement (the lower value of symmetric cost) is used.

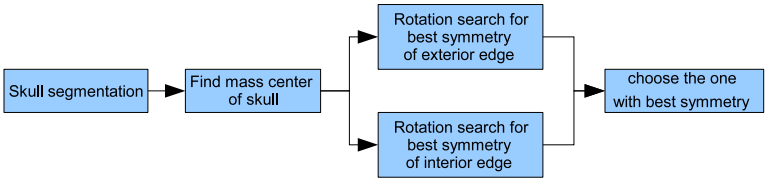

Figure 3.1: Exhaustive symmetric position search.

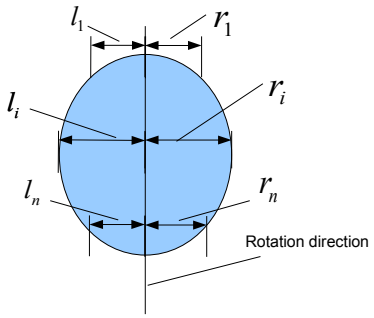

Figure 3.2: Symmetry cost calculation. The l_1 and r_1 actually begins at the top line of the skull (the ellipse), l_n and r_n are actually on the last row of the skull.

Once an approximate midline is estimated using symmetry, brain anatomical features, i.e. the position of the falx cerebri and protrusion of skull bone are used to refine detection.

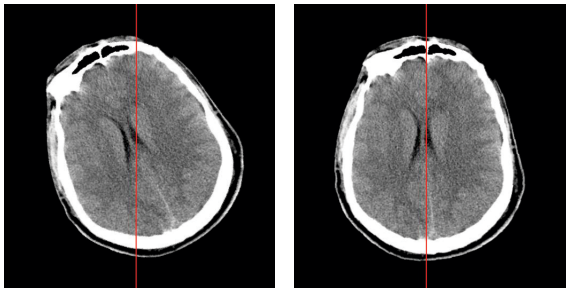

(a) (b)

Figure 3.3: Comparison of different symmetric measurements: (a) using thickness, (b) using center-to-edge distance.

3.2.3 Detection of Falx Cerebri at the Lower Part of the Brain

The falx cerebri is a strong fold of dura mater that follows the fissure between the left and right cerebral hemispheres. In order to detect this anatomical feature quickly and accurately, two searching rectangles are defined based on the ideal midline and the two intersection points with the skull bones. The size of the rectangle is chosen to include the anatomical features to be detected. All the feature processing steps are applied only in these cropped regions of interest(ROI). Figure 3.4 shows the two rectangle ROIs and refined ideal midline based on anatomical features. The method used to detect these features is explained in this and the following sections. First edge detection methods are used to extract the edge map. Hough transform is then applied to detect lines in the edge map. However, this only works if the gray line representing the falx cerebri is very obvious compared to the neighboring region. In some CT images, the area around the gray line has a similar gray scale pattern resulting in unwanted edges in the edge map. To address this issue and erase these edges, first a zero crossing edge detector is used to generate the edge map. This maintains richer edges during Sobel detection and allows removal

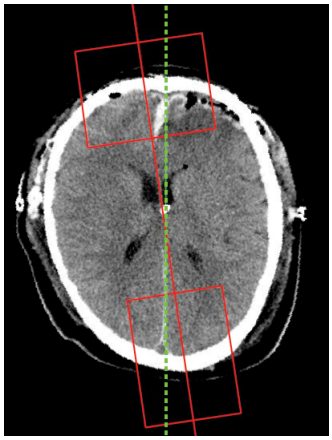

Figure 3.4: Example midline detection result.

of unwanted edges. The edge map is then refined step by step using known features of the falx cerebri. Finally, Hough transform is applied to detect lines representing the falx cerebri. Figure 3.5 shows the schematic diagram. Zero crossing keeps nearly all the edges

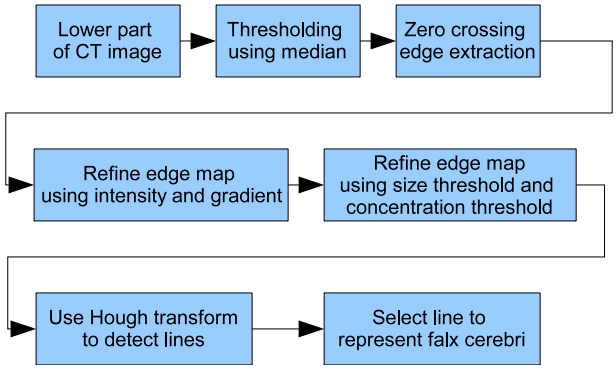

Figure 3.5: Diagram of falx cerebri detection.

regardless of the gray scale values or the sharpness of an edge. Since the aim is to detect light gray lines, not the darker lines, all the gray scale values below the median value of the area are changed to the median. After this step, only the much brighter pixels will retain their original gray levels in the image. This simplifies the edge map generated

later. It was also discovered that the gray line representing the falx cerebri has sharper edges than most other boundaries, and this can be used as a guide to erase trivial edges. This information is incorporated by calculating the Sobel edge map and then applying a threshold to form a revised edge map. The threshold is set as a percentage of the maximal value in the Sobel edge map. Finally, only the edge points that appear in both maps are considered.

Another issue affecting the Hough transform is the presence of small unconnected point clouds close to edges. Hough transform may try to connect them and form a new line. This effect can be erased by removing all edge clouds with points smaller than some threshold value. In this experiment, 3 pixels are used as the threshold.

A final edge point erase is done by only selecting the vertical strips with high edge points along the entire vertical direction. The reason is that after obtaining the approximate position of the midline and rotating the CT images based on this, the gray lines in CT images are mostly vertical. The vertical strip containing the gray lines must therefore have more edge points than other places.

After these filtering steps are applied to the edge map, Hough transform is used to detect lines inside the map. Figure 3.6 displays the entire process. The results of the Hough transform are usually a set of lines. Two constraints must be established to extract the desirable lines from this set. First, the angle of the line must be in the range where the lines are concentrated. This range is obtained by calculating the statistics of the angles of the detected line. Second, the line must lie inside the range where the cluster of lines concentrates. The final ideal midline at this stage is chosen as the longest line satisfying the above constraints.

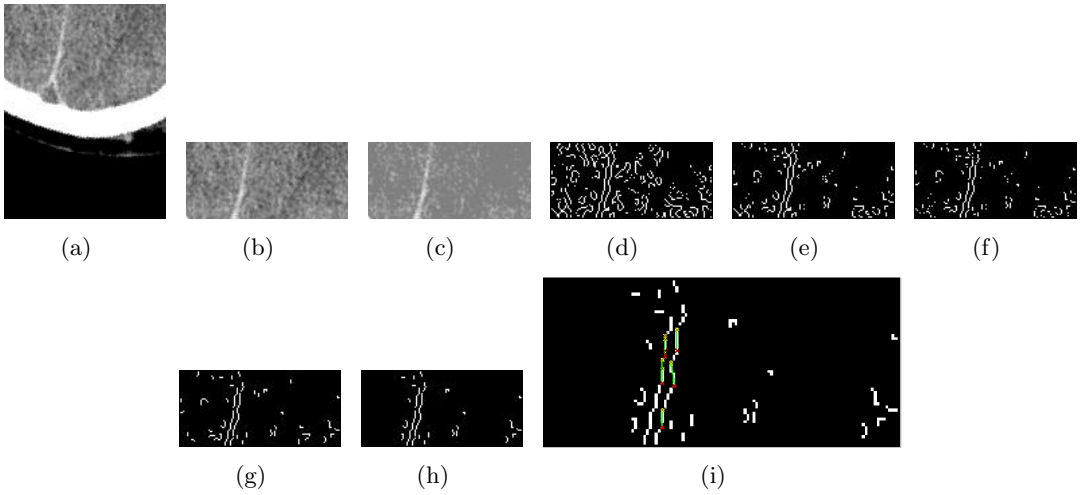

Figure 3.6: Detection of lower falx cerebri. 6(a) The lower part of CT image. 6(b) The lower part without skull. 6(c) Valley filling using median value. 6(d) Edge map after edge detection of zero crossing. 6(e) Edge map masked using intensity threshold on gray scale image. 6(f)Edge masked using gradient threshold on gray scale image. 6(g)Edge map after deleting small connected object. 6(h) Edge map after deleting sparse points. 6(i) Hough transform result on edge map.

3.2.4 Protrusion Detection

A bone protrusion is located in the anterior section of the skull; the falx cerebri extends from this point. This anatomical feature can be used as a starting point for the midline. It can be seen in Figure 3.7 that the protrusion curves down to a local minimum point at the anterior edge of the falx cerebri.

If one views the lower edge of the skull bones as a curve on the image plane, then the curve can be modeled as a 1-dimensional function. Therefore, the protrusion point is the place where the function reaches its minimum. Detection of the protrusion point becomes a matter of finding the minimum of a sampled 1-dimensional function. There are two problems in real images which make this modeling more complex. One is that the protrusion location may not be the global minimum, i.e., the left and right edge may

even be lower than the protrusion place. Therefore the height of bone edge cannot be used directly to locate a local minimum. Another problem is that there are small noisy local minima in other places. In order to address these problems, the derivative is used to find the local minima and a larger neighborhood is searched to avoid small noisy minima. Figure 3.8 explains protrusion detection graphically. Since the derivative is calculated in a discrete curve, obtaining a derivative of exactly zero may not be possible. A suitable alternative is to find the transition point between a negative and positive derivative. Due to the uneven surface of the skull, there may be more than one local minimum inside the region of interest, so the algorithm uses the signed addition of derivatives within a specified neighborhood of the local minimal point. This gives significant preference to large minima over the smaller local minima that occur naturally on the skull surface. If there are multiple large minima in the region of interest, the one closest to the approximate symmetric midline is chosen.

Figure 3.7: The anterior bone protrusion.

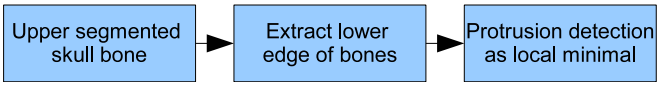

Figure 3.8: Diagram of protrusion detection.

Figure 3.9 shows the curve of a typical bone shape. The aim is to find the point a in the presence of multiple local minima. The difference between point a, the true minimum,

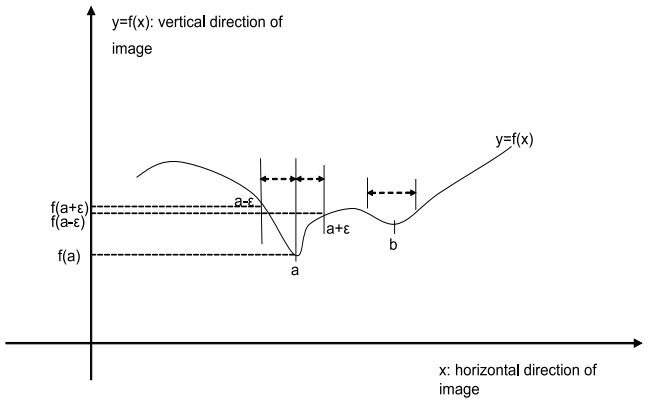

Figure 3.9: Selecting a larger protrusion. Function $f(x)$ is the extracted curve of the interior bone edge.

and b, small protrusion due to irregularity of bones, is the size of the slope around them. This can be captured by increasing the size of neighborhood studied when calculating the derivative; typically the algorithm uses a region of 10 - 15 pixels. The point a is found by searching the maximum of the sum of the left and right derivatives as follows:

$$x_a = arg\max_x [-(f(x) - f(x-w)) + (f(x+w) - f(x))] \tag{4}$$

$$= arg\max_x [f(x+w) + f(x-w) - 2 * f(x)]. \tag{5}$$

where w is the neighborhood width. Equation 5 finds the maximal second derivative. This calculation avoids small amounts of noise around the curve.

3.2.5 Post-processing

The midline detection performs very well where both the anterior bone protrusion and the falx cerebri line are present. In slices where one of these features is not present, the symmetric exhaustive rotation search is repeated with a smaller range and smaller degree steps around whichever feature is present. If neither feature is present, the initial

approximate midline may be used; however, since the skull shape is sometimes complex, the symmetry of the skull will not reflect the true midline. In such cases, slice comparison solves the problem. From the experiment, it is observed that inaccurate midline detection seldom occurs in consecutive image slices, and it is reasonable to assume that the midline should not change much across several consecutive slices of the scan. Using this knowledge, a slice with an "abnormal" midline can be corrected based on the midlines of the slices immediately preceding and following. The adjustment initially identifies the "first class" slices - those with both features detected - then the "second class" slices - those with only one or none feature detected. Then it calculates the angle difference between each second class slice and its closest first class neighbor. If the difference exceeds a certain threshold, the midline is deemed unacceptable, and is replaced with the midline of the closest first class neighbor. The threshold is chosen after some statistical analysis of data observed. This post-processing has two benefits: to guide later segmentation, and to lay a basis for the calculation of structural information after segmentation is complete. Figure 3.10 shows the result of the adjustment based on neighbor slices.

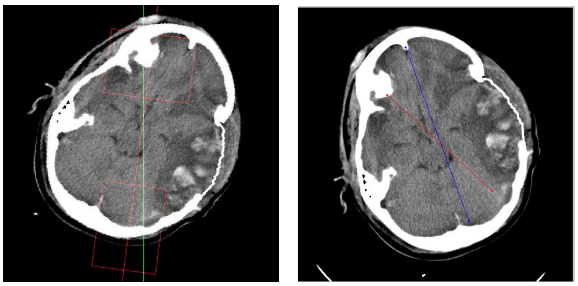

(a) (b)

Figure 3.10: Consistency check: (a) a slice with incorrect midline detection, (b) a corrected slice, where the blue line shows the new midline position.

3.3 Results

3.3.1 Data

The testing CT dataset was provided by the Carolinas Healthcare System (CHS). All subjects were diagnosed with mild to severe TBI when first admitted to hospital. The dataset contains 40 patients. From this set, 391 axial CT scan slices are selected that show ventricles or region that should have contained ventricles. To our knowledge, and based on the literature of the brain CT image processing [46] [78] [103], our database is relatively large, and as a result, the reliability of the testing results for the proposed CT segmentation method should be at least as high as that of almost all comparable works in this field.

3.3.2 Evaluation Criterion

In order to measure the difference between the ideal midline from the proposed algorithm and that of the manual estimation, the following evaluation method is used. Figure 3.11 shows the spatial relations between the ideal midline detected by the algorithm (vertical line) and the ideal midline estimated manually (inclined line). For the manual midline detection process, two points in the upper and in the lower part of the CT slices are recorded and used to identify the manual midline. Then the line segment of the ideal midline detected by the algorithm in the range of the manual ideal midline segment are processed as follows: d_1 and d_2 are the distance between the top two points and lower two points of the two line segments, are used to form the average distance d with respect to the area, i.e., $d = S/h, h = h_1 + h_2$. S is the area enclosed by the two line segments and

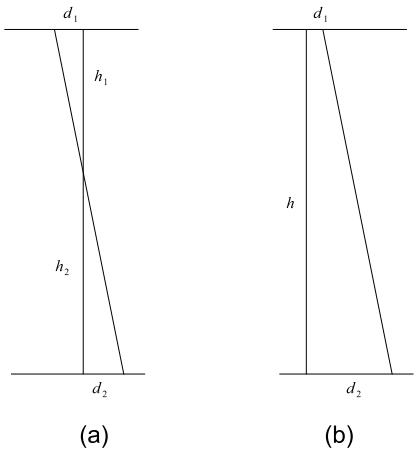

Figure 3.11: Two cases of the difference between the ideal midline detected algorithmically and manually.

the top and bottom line. Finally the difference can be calculated as:

$$d = \frac{d_1 + d_2}{2} \tag{6}$$

for case a in Figure 3.11 and as

$$d = \frac{d_1^2 + d_2^2}{2(d_1 + d_2)} \tag{7}$$

for case b in Figure 3.11.

3.3.3 Results of Ideal Midline Detection

The midline detection algorithm was tested on 391 CT slices. Out of these, 268 slices have the ideal midline in the first class, and 123 have the second class ideal midlines. The ideal midlines were estimated manually by the collaborating physician. Table 3.1 shows the mean and standard deviation of the difference between the algorithm and the manual estimation. As it can be seen in Table 3.1, the proposed algorithm performs very accurately, in particular for the first class midlines, given the fact that the standard

deviation of the manual estimation may be around 1 to 2 pixels. The observation that the algorithm performs better for the first class is understandable because more information is used and processed for the first class of midline. In the detection of the second class, only symmetry and cross slice adjustment are used. In real cases of the second type, the midline usually does not split the skull bone in a symmetrical way. Sometimes there is no gray line in the lower part or obvious separation in the upper part, which can also complicate and compromise the manual labeling and detection of the ideal midline.

Several reasons contribute to a large estimation difference between the algorithm and the expert. Here is a list of them:

- The gray line is too blurry, like a cloud, or no gray line, or no protrusion.
- The protrusion does not correspond to the separating position.
- The gray line in the upper part or a protrusion point in the lower part is used as the reference point.

The first case shows the inherent uncertainty of the problem itself, no algorithm working on the single slice can overcome this. However, by considering neighboring superior and inferior slices may reduce the uncertainty thus result in a good estimation. The second and third cases show the limitations of the proposed algorithm. Further incorporation of anatomical features of used reference points may overcome these limitations.

Table 3.1: The difference between algorithm output and manual estimation in pixel unit

First class	Second class
2.1 ± 1.9	4.0 ± 3.2

CHAPTER 4 Ventricular System Segmentation in CT Images

4.1 Introduction

Research on automated brain CT segmentation is still comparatively scarce. MRI offers improved soft tissue contrast over CT, and is therefore better able to characterize these tissues to aid in segmentation [41]. However, while MRI is suitable for soft tissue examination or in case which can afford long time processing, in real clinical settings, e.g., in traumatic injury case, CT images typically used due to time urgency, better visibility of bones and blood as well as low cost. This emphasizes the need to develop methods for CT image processing. Though CT segmentation has been studied previously, much of the work has focused on cardiac and thoracic anatomy [47, 66, 96], areas for which where CT is a standard method of diagnosis. In [20], a 2D atlas is used for segmentation of abdominal CT volume. Some attempts at segmenting brain CT images have been made. Li et al.[51] devise a method to model spatial relationships between objects in the brain, using General Blackboard (GBB) system to incorporate reasoning based on low lever segmentation and prior knowledge. However, the algorithm was not tested on severe pathological cases. In [56] k-means clustering and neural network are applied to segment areas of hemorrhage in brain CT slices, but the approach is only tested on a single CT slices. In [46] several segmentation methods are evaluated for CT brain segmentation, including intensity based GMM classification, Fuzzy c-Means and Expectation Maximization. The result is relatively good but there is still improvement space for CT segmentation. In this method,

the process is separated into two parts. First an initial low level segmentation method is applied to group pixels into different parts. Then a high level template matching is used to identify ventricles from segmented result. Specifically, ICM and MASP algorithms are adopted for low level CT brain segmentation. Later template matching is employed to further identify ventricle areas.

4.2 Methods

4.2.1 Low-level Segmentation

In CT scans, the ventricle system typically has darker color than other tissue. A simple method to segment ventricle would be using binary thresholding, with the threshold value chosen via Otsu's method [69]. However, testing this method gave poor results, with severe noise and object fragmentation. The challenge is that in CT scans there are many "holes" or noise (which has different gray scale values) in tissue areas. Another challenge is that the boundary between different tissue parts is very blurry. Binary segmentation is also unrealistic since there are multiple tissue types within the brain. Furthermore, simple thresholding classifies each pixel independently of its neighbors. This cannot work well when different tissues have wide range of overlap of gray scales. To address the problem of noise and blurry boundary, segmentation methods adopted here follow conditional probability models where the most probable label of a pixel depends upon the attributes of both the pixel itself and its neighbors. In this study, two such spatial segmentation methods are evaluated: Iterated Conditional Models (ICM) [6] and Maximum A Posteriori Spatial Probability (MASP) [50].

For both methods, some starting assumptions are made. It is assumed that each pixel x in an image $\mathbf{X}$ has an attribute l_x representing the label to which it is assigned, and

an attribute g_x representing its gray-level intensity. This gives rise to two subimages $\mathbf{L}$ and $\mathbf{G}$, where $\mathbf{L} = l_x, x \in X$ and $\mathbf{G} = g_x, x \in X$. $\mathbf{G}$ is the observable image of gray-level values, and $\mathbf{L}$ is the 'hidden' image of assigned labels. The labels in $\mathbf{L}$ each take some value $k \in K$, where K is the number of distinct objects (or tissue types) in the image. Except for those on the image border, each pixel x has M neighboring pixels, and these form a neighborhood $N_x = (x^{(1)}, x^{(2)}, ..., x^{(m)})$. This is split into a neighborhood label configuration $N_l = (l_x^{(1)}, l_x^{(2)}, ..., l_x^{(m)})$, and a neighborhood gray-level configuration $N_g = (g_x^{(1)}, g_x^{(2)}, ..., g_x^{(m)})$. The set of all possible neighborhood configurations is denoted by $\mathbf{N}$. Usually 4-neighborhood or 8-neighborhood are used. Figure 4.1 shows the 8-neighborhood gray-scale block and label block in a image. Generally, in our application, four types of brain matter - bone or blood, ventricular tissue, and light and dark grey matter - are assumed to represent different ranges of gray scale in the brain.

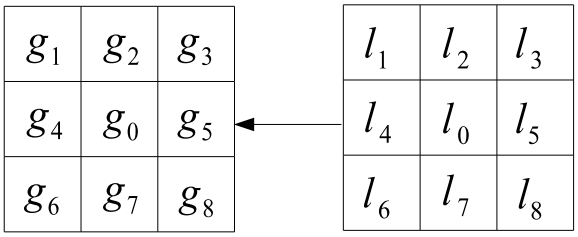

Figure 4.1: Gray scale grid and label grid of images.

In using the spatial information in each pixel's neighborhood, two assumptions are made. First, that the gray scale value g_x of pixel x depends only on the label of x and not its gray-scale neighborhood, i.e., g_x and N_g are independent given the label l_x. Second, the dependence between the labels are local. ICM and MASP have different assumptions on local dependence.

Iterated Conditional Modes (ICM)

ICM [7] follows the two assumptions made about spatial segmentation: a pixel's gray scale value g_x is dependent only on its label l_x and not the values of other pixels given the label $l_(x)$; the ideal label map L^* is a realization of a locally dependent Markov Random Field with distribution $p(x)$. The statistics of each label class are computed using the Gaussian model, so each class has parameter set the mean μ_k and the variance σ_k which can be estimated from the image. Therefore the conditional density of the image G_x given L_x is given by the following due to independence assumption.

$$l(G_x|L_x) = \prod_{i=1}^{n} f(g_{x_i}|l_{x_i}) \tag{8}$$

ICM iteratively finds a local maximum of $P(L_x|G_x)$, updating each pixel's label in every cycle, which can be expressed in the following Equation:

$$\hat{l}_x = arg\max_k P(x = k|g, N_c) \tag{9}$$

Suppose that $\hat{L}$ is a provisional estimate of the true label map L^*, and at each step the estimated $\hat{l_x}$ is updated at each pixel x given all available information. For each pixel x, denote $x = k$ meaning that pixel x has label $k, k = 1 \cdots K$. Denote g the gray-scale value of x, N as one of the neighborhood labels configuration of x and N_c the current estimation of neighborhood configuration, which is from $\hat{L}$. G is the gray-scale values of x's neighborhood. By using the two assumptions, Equation 9 can be written as

$$P(x = k|g, N_c) \propto f(g|x = k)P(x = k|N_c), \tag{10}$$

where $f(g|x = k)$ is the probability of a pixel x having a particular gray-scale value g given

its label k, and $p(x = k|N_c)$ is the probability of being label k given the labels of its current estimated surrounding neighbors N_c. A single cycle applies this to each pixel in turn, and the cycle is repeated until the estimated label map $\hat{L}$ does not change significantly between iterations.

Note that the ICM method requires initial segmentation of the CT image. Here k-means is used, due to its speed and reasonably accurate performance. The initial seeds are chosen manually, after using training examples to calculate a standard gray scale range for each type of brain tissue. These ranges are consistent across the majority of images, and k-means initialization is therefore satisfactory.

Maximum A Posteriori Spatial Probability (MASP) Segmentation

As in ICM, there are also two assumptions in MASP [50] segmentation algorithm. First is the same independence assumption about the gray-scale value given the label of the pixel. Second is about local dependence of labels. The neighborhood configuration depends on which class or label the center pixel belongs to. Use the same notation as in ICM section, MASP tries to label each pixel using the following formula:

$$\hat{l}_x = arg \max_k P(x = k|g, G), \tag{11}$$

where

$$P(x = k|g, G) = \frac{P(g, G|x = k)P(x = k)}{P(g, G)}. \tag{12}$$

Since $P(g, G)$ is independent of the label k, we have

$$P(x = k|g, G) \propto P(g, G|x = k)P(x = k). \tag{13}$$

Calculating $P(g, G|x = k)$ requires more effort. By using the law of total probability, $P(g, G|x = k)$ can be used to calculate as follows:

$$P(g, N|x = k) = \sum_{N_l \in N} P(N_l|x = k)P(g, G|x = k, N_l), \tag{14}$$

which, using assumption 1, can be written as

$$\begin{aligned} & P(g, N|x = k) \\ & = \sum_{N_l \in N} P(N_l|x = k) f(g|x = k) \prod_{m=1}^{M} f(g_m|x_m \in N_l). \end{aligned} \tag{15}$$

It also assumes that $f(g|x = k)$ follows a normal distribution with parameters μ_k, the mean grey-level for class k, and σ_k, the standard deviation of the gray-scale values for class or label k.

Modified MASP

In this section our modified version of MASP, used in this study, is described. The computational demands of the conventional MASP process can be significant. Since the algorithm averages probabilities over all possible neighborhoods in Equation 15, its dimension increases rapidly with more complex images. A simple binary segmentation using a 4 pixel neighborhood has a dimension of only $2^4 = 16$. However, CT image segmentation is more complicated for two reasons. Firstly, at least 4 labels are required: bone, ventricle tissue, and light and dark grey matter. Secondly, as mentioned before, if we use an 8-pixel neighborhood, the resulting dimension is therefore $4^8 = 65536$ which is a very large number for probability estimation. Moreover, the MASP algorithm is applied iteratively to each individual CT slice, taking around 8 iterations on average, and each slice contains $512 \times 512 = 262144$ pixels, with up to 8 slices per patient scan. All these result in very

long computation time for MASP. Since speed is vital when medical decisions must be made quickly, this high dimension results in unacceptably slow performance. In [3], we proposed that instead of averaging the probabilities over all neighborhood configurations, the current estimation of labels can be used. The modified MASP algorithm uses only the current estimated neighborhood for the each pixel. In this case, instead of calculating $P(g, G|x = k)$, it actually calculates $P(g, G, N_c|x = k)$ as follows:

$$P(g, G, N_c|x = k) = P(N_c|x = k) \times p(g, G|x = k, N_c). \tag{16}$$

From the independence assumption, we have

$$P(g, G, N_c|x = k) = P(N_c|x = k) f(g|x = k) p(G|N_c) \tag{17}$$

$$\propto P(N_c|x = k) * f(g|x = k). \tag{18}$$

The modified algorithm significantly improves the segmentation speed for each individual slice, with no obvious negative impact on performance.

4.2.2 High-level Template Matching

After initial low-level segmentation, the image pixels are grouped into different types of tissue. Since initial segmentation only relies on gray scale and highly local neighborhood information, this leads to poor performance on pathological CT images, as they may contain bruised tissues which are very similar to ventricle matter in terms of local neighborhood intensity statistics. However, the use of templates can improve the discrimination between the two different tissue types by considering the location as a feature. The schematic diagram of ventricle identification from initial segmentation result is shown in Figure 4.5. First, a size threshold is applied to all candidate ventricle objects to remove

noise and small artifacts. In experimental results, it was observed that non-ventricular objects that resemble ventricles, i.e. bruise area, often appear very close to the edge of the brain. Two bounding boxes are therefore used to exclude these objects; one large and one small, both centered in the middle area of the skull. The small box applies the constraint that all ventricle parts should be inside a certain area of the brain; the large box applies the constraint that all ventricle parts should not exceed a certain area bound. If some portion of a candidate object falls outside of the large bounding box, or some portion does not fall within the small bounding box, the object is rejected. The sizes of the two boxes were determined via experimental analysis on a training set of CT images.

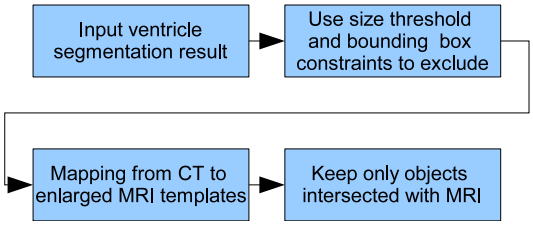

Figure 4.2: Diagram of ventricle recognition.

Though the bounding boxes successfully reject most non-ventricular objects, some are too close to the true ventricles to be excluded. Since the shape and position of the ventricles changes across the multiple slices in a full CT scan, if the position of the current slice in the sequence is known then more precise constraints can be used. For example, provided the full CT scan set is available, the location of a specific CT slice in the brain can be determined based on the resolution of the direction perpendicular to the axial plane (referred to as the z direction) and the order of the slice. The brain atlas information can be used to obtain the ventricle shape information at that specific location. The algorithm in

this study use a brain MRI template set[1] to extract ventricle shape information. The fourth ventricle is not considered in this work because it is rarely used to measure the midline shift, however the same principle can be applied for the fourth ventricle recognition. Due to the resolution difference between CT scan and MRI scan, a slice order mapping between these two sets are required. Figure 4.3 illustrates this mapping. Once the mapping of a

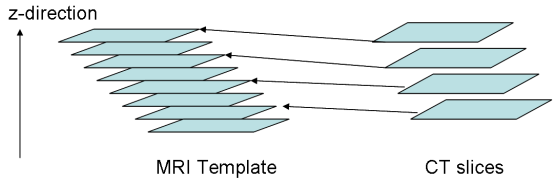

Figure 4.3: Mapping between MRI template and CT slices.

CT slice to a MRI ventricle template is known, it can be applied for the majority of all other CT slices. While the resolution of the CT scan depends on the CT machine type and settings, the resolution for a given set of scans is fixed. In addition, the ventricle systems in the z-direction does not show significant variation across the training set. Therefore, mappings can be approximated with linear form. In the method described here, these mappings are first initialized manually and then optimized using a set of training images. Due to the slight variance in ventricle position as well as ventricle deformation across multiple patients, the original MRI template is enlarged via morphological dilation. The enlarged template provides an estimation of the position of ventricles. Figure 4.4 shows the enlarged MRI templates.

After selecting the specific MRI template through slice mapping between CT scan and MRI scan, the template is aligned with the CT slice. The alignment is largely simplified by

[1]The template is generated based on the annotated images from the Digital Anatomist Interactive Atlas of University of Washington, http://da.biostr.washington.edu/da.html

Figure 4.4: MRI template set after dilation.

using calibrated CT scans from the ideal midline detection step, because there is no need to rotate images for alignment. The template is resized to make sure that the bounding box of the MRI template (which is the minimal rectangle covering the object) and the bounding box of the CT scan are the same size. Any candidate segment that intersects with the template is accepted as ventricular object. Figure 4.5 shows an example of the ventricle recognition step. From the results, one can see that the ventricle parts are successfully recognized using size, bounding box and template constraints.

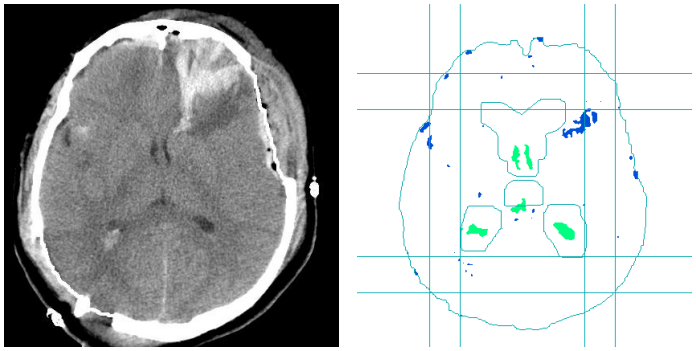

(a) Original CT image (b) Ventricle segmentation result

Figure 4.5: Results of ventricle detection using bounding box constraints and template matching. The segmented objects intersected with the enlarged template are recognized as ventricles.

The advantage of the proposed ventricle detection method over existing image segmentation approaches is that it incorporates anatomical knowledge into the detection procedure such as in the detection of the ideal midline. In ventricle recognition, prior

information is embodied in spatial templates derived from MRI images.

4.3 Results

4.3.1 Data

The testing CT dataset was provided by the Carolinas Healthcare System (CHS). All subjects were diagnosed with mild to severe TBI when first admitted to hospital. The dataset contains 40 patients. From this set, 391 axial CT scan slices are selected that show ventricles or region that should have contained ventricles. To our knowledge, and based on the literature of the brain CT image processing [46] [78] [103], our database is relatively large, and as a result, the reliability of the testing results for the proposed CT segmentation method should be at least as high as that of almost all comparable works in this field.

4.3.2 Analysis of ICM and MASP

Since both ICM and MASP use spatial neighborhood information and probability model in their algorithm, it is interesting to compare these two algorithms. In the following we analyze the similarity, differences and their link between these algorithms.

Similarity

One of the two assumptions in ICM and MASP is the same, which assumes that given the label of the pixel, its gray scale value is independent of other neighborhood labels. For the other assumptions in ICM and MASP, the common points are that both assumptions assume local neighborhood dependence. In sum, both methods assumes a two layer way of viewing images. The higher layer is the label grid for each pixel location, the lower layer is the actual image based on Gaussian distribution for each label.

Differences

The ICM assumes Markov Random Field model to generate the label grid. This means that the model is expressed as $p(x = k|N)$, where x is the center label and N is the neighborhood labels configuration. MASP, however, assumes that the neighborhood depends on the center pixel, which can be expressed as $p(N|x = k)$. The directions of dependence is the main difference between these two methods. Other differences are the calculations made to estimate these probabilities. In ICM, $p(x = k|N)$ is calculated using a defined probability function, e.g., using ratio of labels in the neighborhood to calculate the probability function. In MASP, the probability $p(N|x = k)$ is estimated from the image by counting the proportion of each pattern. If the number of distinct labels K is large, MASP is computationally expensive because the number of neighborhood pattern is K^n, where n is the number of pixels defined in neighborhood.

Relationship between ICM and MASP

It can be proved that the objective functions used in modified MASP as in 4.2.1 and ICM are equivalent, the only difference is the different approaches to evaluate conditional probability functions based on the different assumptions made in the two cases. For ICM, the probability function being evaluated is

$$P(x = k|g, N_c) \propto f(g|x = k)p(x = k|N_c) \tag{19}$$

Modified MASP attempts to maximize the following function with different label k:

$$P(x = k|g, G, N_c) \propto P(x = k)P(N_c|x = k)f(g|x = k) \tag{20}$$

$$= P(x = k, N_c)f(g|x = k) \tag{21}$$

$$= P(x = k|N_c)f(g|x = k)P(N_c) \tag{22}$$

$$\propto f(g|x = k)P(x = k|N_c) \tag{23}$$

$$= P(x = k|g, N_c) \tag{24}$$

As it can be seen, in terms of formal expression, both ICM and modified MASP try to maximize the probability of $P(x = k)$ conditioned on its gray scale g and its current estimated neighborhood N_c. The difference between modified MASP and ICM are that ICM use MRF to model the probability function $P(x = k|N_c)$, which is later estimated using current estimated labels, modified MASP use the current estimated labels directly to estimate the probability $P(N_c|x = k)$. Since they both use the same objective function to choose labels, ICM and modified MASP should have similar labeling result. However, because the large space of neighborhood configuration, using image data for probability estimation may not be sufficient. Therefore ICM seems a safer method of using spatial information.

Illustration on CT Data

In order to assess and compare the performance of the segmentation algorithms, we apply both methods on the CT dataset. For ICM, the simplest non-degenerated MRF is used and $\beta = 1.5$ [7]. For MASP and modified MASP, 8-neighborhood is used. Each algorithm runs for 10 iterations, given a starting label map generated via k-means with fixed seeds

initialization. As a baseline, K-means result is also presented. The difference between K-means, ICM, MASP and modified MASP can be seen in Figure 4.6. From the result we

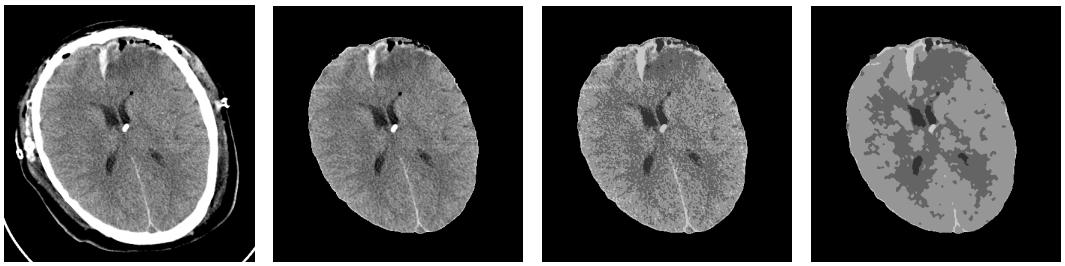

(a) Original CT image (b) CT Image without skull (c) K-means (d) ICM

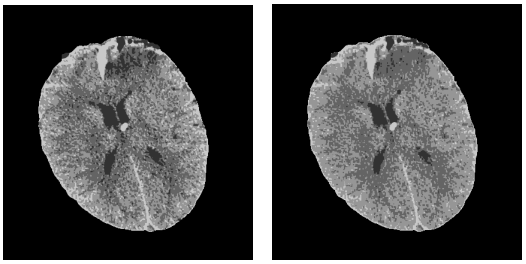

(e) MASP (f) Modified MASP

Figure 4.6: Comparison of Segmentation methods

can see that ICM, MASP and modified MASP have smoother effect than simple K-means. This is due to the incorporation of local neighborhood information into labeling pixels. Compared to MASP, ICM has very clear boundary and shows a suitable performance dealing with noise. However, due to the smoothing effect, ICM also loses some detailed information, e.g., the upper horn on the lateral ventricles. MASP tends to maintain more details in segmented result, however it also keeps noisy part inside. For example, on the upper right corner, a part of the bruise region is classified as ventricle class. Since modified MASP has similarity with both ICM and MASP, it shows intermediate segmentation result, i.e., it shows more noise than ICM while keeping some detail of horns. However, it has less noise than MASP. Testing results on other CT images show similar characteristics of

these algorithms.

4.3.3 Results of Ventricle Segmentation

Since ICM is faster and has smoother result than MASP, ICM is used as our low-level segmentation method for evaluation of the proposed entire ventricle segmentation method. Then template matching method is used to recognize ventricles. Evaluation of final ventricle recognition was done by visual inspection conducted by the participating physician. Here two measurements are defined to evaluate the result. The first is a sensitivity-like measure. It is the rate of slices in which ventricular regions are correctly detected as ventricle. The second is a false positive-like measure. It is the rate of slices in which non-ventricular regions are incorrectly detected as ventricles. The sensitivity-like measure, denoted as M_s, and the false positive-like measure, denoted as M_f, can be illustrated in the following equations:

$$M_s = S/N, \tag{25}$$

$$M_f = F/N, \tag{26}$$

where N is the total number of CT slices, S is the number of slices in which ventricular regions are correctly detected, F is number of slices where non-ventricular regions are detected as ventricles.

In the experiment, for the sensitivity-like measure, the rate is 100% because all ventricles are identified in all slices. The false positives-like measure is 8.59%, i.e., 33 out of 391 slices have falsely classified ventricles. These false positive objects in CT slices either included non-ventricle objects, e.g. areas of edema, or detected objects in slices where no ventricles were originally visible, which implies some mismatch between the adopted

segmentation method and segmentation based on physician's interpretation. The impact of these false positive objects may mislead the actual midline using shape matching later. Thus it is very important to control the false positive low enough.

4.4 Conclusion

This study provides a method for automatic ventricle segmentation as well as an ideal midline detection algorithm using axial head CT images. First, an accurate ideal midline detection method is proposed, and used to correctly align the scan set based on the ideal midline. This is crucial step before using any template matching later because it avoids the need to shift or rotate templates, and therefore simplifies registration. Then low-level segmentation and high-level ventricle recognition using template matching are applied. Our method offers the following improvements over existing approaches: accurate detection of ideal midline, ventricle recognition using both anatomical features and spatial templates derived from MRI images. In addition, ICM and MASP are analyzed and compared both mathematically and experimentally. The relatively large size of the CT dataset used for testing makes the results of this study more reliable.

CHAPTER 5 Gaussian Mixture Model (GMM) Based Initial Low Level Segmentation in CT Images

5.1 Introduction

The work presented/proposed in this chapter intends to further improve the initial low-level segmentation in brain CT images using Gaussian Mixture Model (GMM). The GMM method was first used for segmentation of noisy MRI scan in [29]. This work adopts the Gaussian Mixture Model (GMM) [29] method to segment ventricular system in brain CT scans. The results are compared with K-means clustering based segmentation and Iterated Conditional Modes (ICM) [6]. The difference between GMM used here and other simple Gaussian modeling methods is that it uses both intensity value and location features. Furthermore, each part is modeled with multiple Gaussians which makes it capable to model concave shapes. Generally, The GMM method has the following benefits:

- GMM can provide smooth boundaries
- GMM can easily incorporate prior information, such as location and texture information
- GMM models different parts naturally

These benefits will be explained by analyzing experiment results.

5.2 Methods

5.2.1 Gaussian Mixture Model for Image Segmentation

An image is composed of individual pixels. There are very close relations between neighboring pixels, such as similar intensity values. Because the composition of a meaningful image is not a random combination of pixels, pixels can be grouped together according to similar features. This will increase the granularity of representation. The Gaussian Mixture Model assumes that each segmentation part can be modeled as one or more Gaussian distributions. A simple example of GMM application is background and foreground segmentation based only on intensity value. An image background typically has very similar local intensities. The same thing is assumed for foreground. It is also assumed that the intensity overlap between foreground and background is small. The intensity distribution of background and foreground can therefore be modeled using multiple Gaussians. In this work, the same idea is adopted for modeling different parts of brain tissue in CT images. This application considers not only the intensity value, but also the location feature of each pixel. Therefore, each Gaussian is actually a multivariate Gaussian distribution.

To estimate the Gaussian Mixture Model parameters, the Expectation-Maximization (EM) [19] algorithm is used to adaptively learn all parameters starting from some initial values. The main idea of the GMM method used here is described in [29], where it is called Constrained Gaussian Mixture Model (CGMM). In [29], GMM is applied for noisy MRI images segmentation. Compared to MRI scan, CT scans have more noise, therefore the GMM method is expected to offer good performance on CT images too. The following section will explain the use of the GMM method for image segmentation.

GMM and Parameter Estimation

The Gaussian Mixture Model has the following probability distribution for each sample point, i.e., each pixel,

$$f(v_t|\Theta) = \sum_{i=1}^{n} \alpha_i f_i(v_t|\mu_i, \Sigma_i), \tag{27}$$

where v_t are feature vectors of pixel t. In this study, the vector includes location and intensity values. Θ represents the model parameters including α_i, μ_i and $\Sigma_i, i = 1, \cdots, n$. Parameter n is the total number of Gaussian distributions, α_i is the weight controlling the contribution of the ith Gaussian, and μ_i and Σ_i are the corresponding mean value and covariance matrix of the ith Gaussian. Since both location and intensity information are used, the parameters can be decomposed in the following manner:

$$\mu_i = \begin{pmatrix} \mu_i^{XY} \\ \\ \mu_i^{I} \end{pmatrix} \quad \Sigma_i = \begin{pmatrix} \Sigma_i^{XY} & \Sigma_i^{XYI} \\ \\ \Sigma_i^{XYI} & \Sigma_i^{I} \end{pmatrix} \tag{28}$$

The superscripts XY and I mean location coordinate values and intensity value respectively. Equation 27 gives the probability of a certain pixel's appearance with feature v_t. Suppose there are k different parts to be separated in an image, and each part is modeled by $l_i, i = 1, \cdots, k$ Gaussian distributions. The value of interest is the posterior probability $p(v_t \in part_j|v_t)$, as this decides which part the pixel is most likely to belong to (maximizing *a posteriori* probability). The equation for calculating the posteriori probability will be explained in 5.2.3.

In the GMM used in this work, a constraint can be put on the covariance parameters. It is assumed that there is no dependency between the location parameter and the intensity parameter. This assumption is natural because a part can have arbitrary shape indepen-

dent of its intensity values. This reduces the number of parameters to be estimated. There are several options to decide Gaussian relation with each other. First, all Gaussians can have their own independent mean and covariance matrix. So in the EM training step, all these parameters will be updated independently. Another way is to consider all Gaussians belonging to the same part as sharing similar intensity value, so the intensity component in the mean parameter of the same part will remain the same for each update. In this case, intensity covariance can be updated independently or together with all Gaussians in the same part. The algorithm presented here follows the approach used in [29], which keeps both mean and covariance of intensity parameters the same for a single part. For the location component in mean and covariance, every Gaussian is updated independently, since the shapes of one part in different locations are not related.

In order to describe the connection between Gaussians and the tissue parts, a mapping between the Gaussian distribution index and the part index is introduced. Define $\pi : 1, \cdots, n \rightarrow 1, \cdots, k$ as the mapping from the index set of Gaussian to the index set of tissue parts. With the assumption of independence between intensity feature and location feature in each Gaussian, the parameters in GMM can be described as follows:

$$\mu_i = \begin{pmatrix} \mu_i^{XY} \\ \\ \mu_{\pi(i)}^{I} \end{pmatrix} \quad \Sigma_i = \begin{pmatrix} \Sigma_i^{XY} & 0 \\ \\ 0 & \Sigma_{\pi(i)}^{I} \end{pmatrix} \tag{29}$$

Once an initial estimate of each parameter has been calculated, the EM method [19] can be used to update each parameter iteratively. The detailed equations can be found in [29]. The EM method is known to be very sensitive to the initial values, so suitable initialization of these parameters is crucial.

5.2.2 Initialization of Gaussian Mixture Model

This first step determines the total number of Gaussians, the means, the covariance matrices, the weights and their associated part index. This section will briefly explain initialization; a more detailed description can be found in [29]. Since the intensity value of each pixel has a corresponding physical meaning, this should be counted as primary information for segmentation. This naturally leads to the use of K-means to group pixels based on intensity value. Since the number of tissue parts in CT images does not change significantly, the number of clusters can be considered fixed. This alleviates the main challenge in clustering - i.e. how to decide the number of clusters. This study uses 4 clusters to model skull and blood, ventricular tissue, dark gray tissue and light gray tissue. For each clustered region, a criterion is applied to test each non connected region to check how much percentage of that part is in its inscribed ellipse. If the percentage is larger than a threshold value, the region is represented by a single Gaussian. Otherwise the region is split into two regions based on K-means separation based on location. This is a top down procedure to make sure every region is well represented by a Gaussian distribution. Figure 5.1 shows the results of K-means initialization and Gaussian parameter estimation.

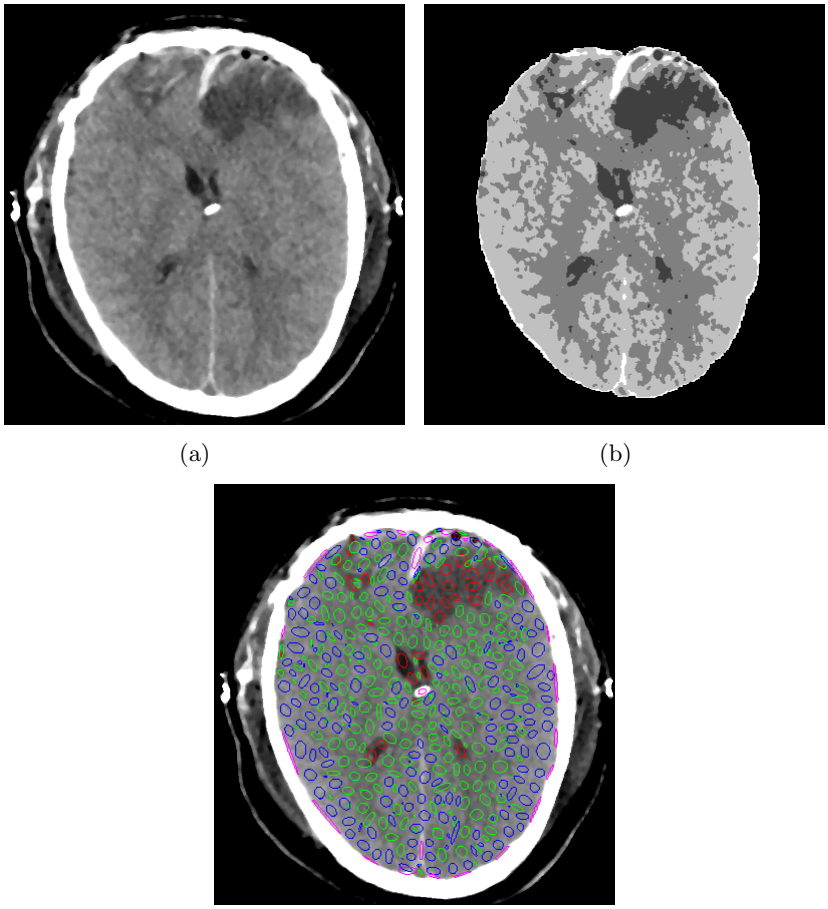

(a) (b)

(c)

Figure 5.1: Figure 1(a) is the original CT image with smooth Gaussian filtering. Figure 1(b) is the segmentation result with K-means. Figure 1(c) is an illustration of Gaussian initialization, where each ellipse represents 1σ size in each direction.

5.2.3 Segmentation based on Probabilistic Model

After all parameters are estimated using EM, the posterior parameters can be calculated using the Bayes rule.

$$p(part_j|v_t) = \frac{p(v_t, part_j)}{p(v_t)} \propto p(v_t, part_j) \tag{30}$$

$$p(v_t, part_j) = \Sigma_{i \in \pi^{-1}(j)} \alpha_i f_i(v_t|\mu_i, \Sigma_i), \ j = 1, \cdots, k. \tag{31}$$

In Equation 31, $\pi^{-1}(j)$ returns all Gaussian indexes belonging to part j. Then the most probable label for pixel v_t is

$$part\_label_t = \arg \max_{j \in 1,\cdots,k} p(v_t, part_j) \tag{32}$$

Figure 5.2 presents the segmentation results after each iteration of EM. The CT image used is the same as in Figure 5.1.

5.2.4 Ventricle Recognition

GMM segmentation is a very low level segmentation procedure. It is based on intensity value and Gaussian blob modeling to prevent abrupt label changes. However, not all Gaussians with similar intensity value correspond to the same tissue type in brain CT images. For example, in CT images from TBI cases, there are often bruised areas which have very similar intensity value to ventricular tissue. There are also air blobs in the brain, which appear as dark areas in CT images and will be grouped as ventricles by GMM. More information is required to separate these parts from ventricles. Since ventricles have an approximately fixed position in the brain, a template to represent this location information can help separate them from non-ventricle parts. This study applies the same strategy as in [14]. Three constraints are used to exclude non-ventricle parts:

- Constraints on the size of segmented region
- Constraints on the location of ventricles using the brain bounding box
- Constraints on the location of ventricles using the ventricle template

The size constraint removes small noise, fragmented part. The brain bounding box excludes most of the bruised areas because they often occur close to the skull boundary. The ventricle template provides more accurate location information to exclude non-ventricle areas. The ventricle templates are extracted from a standard brain MRI scan and are enlarged using morphological dilation to accommodate variations among different subjects and pathological cases. Figure 5.3 shows a set of template images. Figure 5.4 illustrates the ventricle recognition result of one CT slice.

5.3 Results

5.3.1 GMM Results and Comparison with other Methods

This section compares the results of the GMM method with ICM and K-means. Prior to segmentation, a median filter is applied to all CT images. This results in smoother segmentation using K-means clustering. Both ICM and GMM use the K-means segmentation for initialization; the model parameters are then estimated and updated iteratively.

The test CT dataset is provided by the Carolinas Healthcare System (CHS). All subjects were diagnosed with TBI. The dataset contains 40 patients, and 391 axial CT scan slices are selected from regions where the ventricles typically appear. The size of each CT slice is 512*512 pixels.

The results are evaluated manually via visual inspection. In general, the GMM method achieves better segmentation than ICM and K-means.

Figure 5.5 presents several CT image segmentation results using different methods. From the results it is clear that GMM provides better separation of close objects. K-means merges close objects together since it is only based on intensity value, and leaves small holes in other parts. ICM merges close objects due to the neighborhood label

having bigger influence than its a pixel's own intensity value. Large close objects with the same label therefore tend to merge together. The GMM method includes the location information and allows different labeled regions to compete for territory. In the presented example, the gap will not simply shrink but compete with other close objects to gain more territory. Since posterior probability is based on both intensity value and location, larger close parts with other label may not have high probability in terms of location feature.

5.3.2 Complexity Analysis and Speed Improvement

The most time consuming component of the GMM model is parameter estimation using EM. In the Expectation step (E-step), the probability of each pixel with each Gaussian must to be evaluated. Suppose there are n Gaussians and the image pixel number is T; the probability must then be calculated $n * T$ times. Each calculation involves a multivariate Gaussian probability evaluation, which is time-consuming compared to other operations. However, for each Gaussian only close pixels will be influenced. As the distance increases, the probability value decreases exponentially. Based on this observation, the probability of pixels only needs to be calculated within a certain range, say 10σ away from the mean location, where σ is half length of the main axis of the ellipse shape based on each Gaussian's covariance matrix. This improves the segmentation speed considerably. In this study, for a CT image with 500 Gaussians, it takes about 3.5 minutes to finish 4 iterations on a desktop computer with a dual core 3GHz CPU and 4GB of RAM . There are also other sophisticated ways to further improve the speed of GMM evaluation, e.g., many methods are provided in [11].

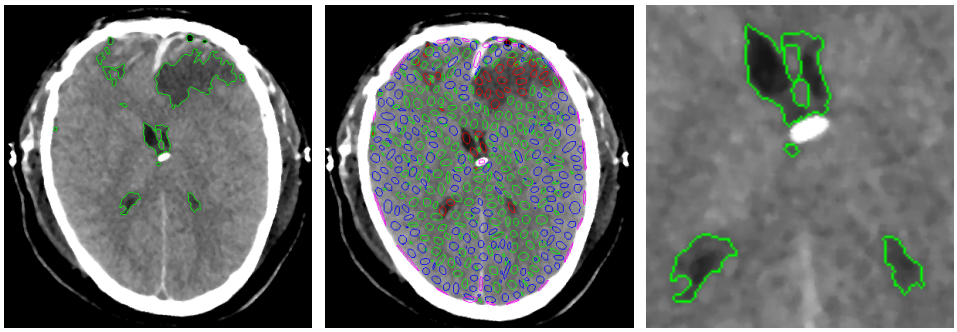

(a) initial state

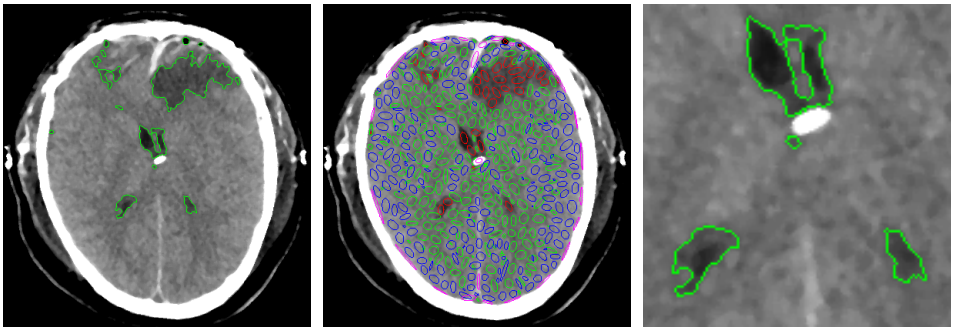

(b) iteration 1

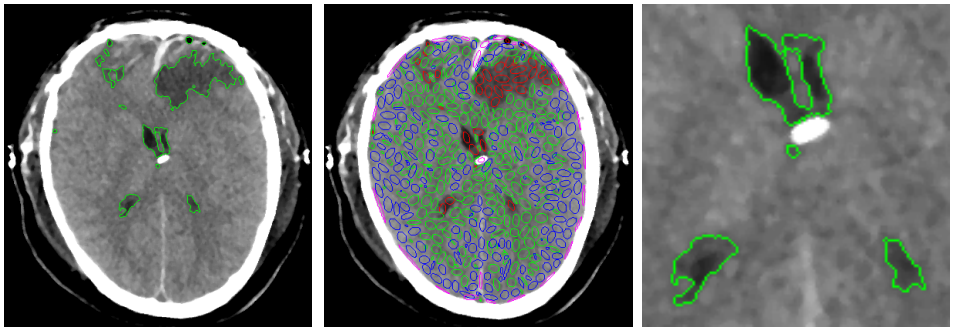

(c) iteration 2

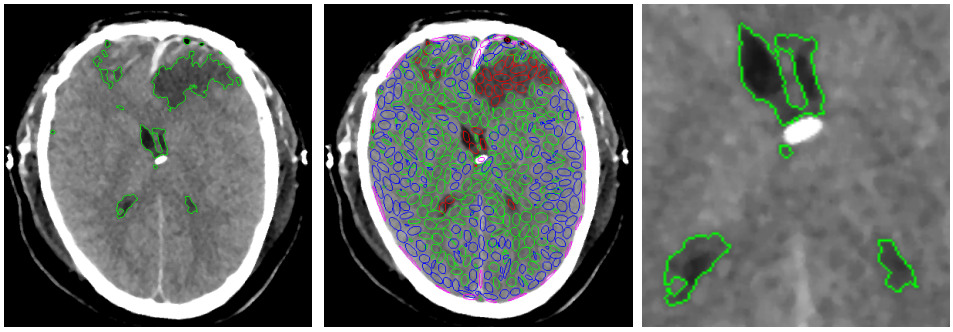

(d) iteration 3

Figure 5.2: Iterative EM update and corresponding segmentation result. As can be seen in the figure, GMM method separates the upper lateral ventricles successfully. Another change is that the lower left part of ventricle is growing into a round shape. This illustrates GMM's ability to control the segmentation result using regular or simple shape. This feature of GMM controls the complexity of boundaries and thus leads to relatively smooth segmentation results with certain initialization granularity.

Figure 5.3: Enlarged ventricle templates extracted from brain MR images.

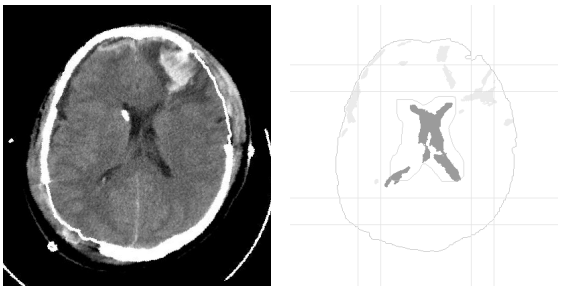

(a) CT images (b) Recognized Ventricles

Figure 5.4: Ventricle recognition result. Skull edge, bounding box and ventricle template are outlined. Ventricles are shown as dark gray. Other parts with similar intensity value are excluded based on constraints and are shown in light gray color.

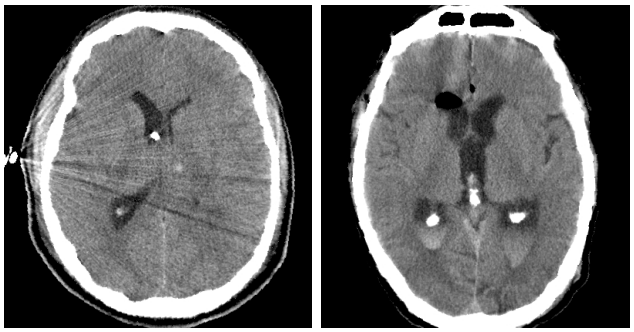

(a) CT image

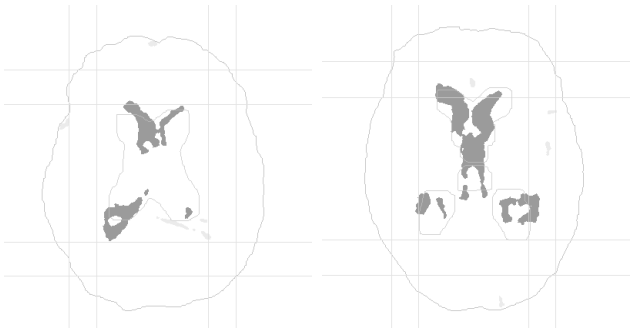

(b) GMM result

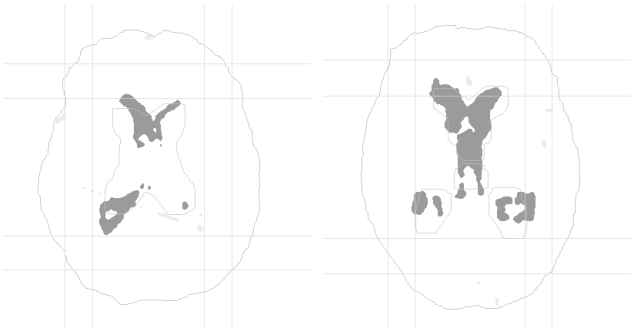

(c) ICM result

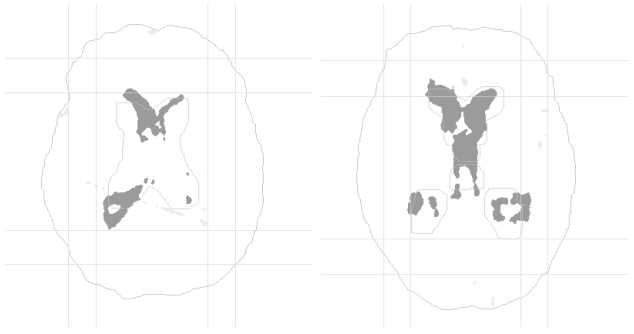

(d) K-means result

Figure 5.5: Ventricle segmentation results of GMM, ICM and K-means. GMM separates the upper pair of lateral ventricles better than ICM and K-means.

CHAPTER 6 Actual Midline Estimation Using Shape Matching and Midline Shift Calculation

6.1 Introduction

Based on segmentation of ventricles, the actual midline that lies between the left and right lateral ventricles or through the third ventricle can be estimated for midline shift measurement. Due to many factors such as poor quality of CT images, the result of such segmentation processes is often inaccurate and includes artifacts such as false positives and missing parts, as shown in Figure 6.1. The variations of ventricle shapes also complicate the estimation of actual midline. For the slices that include lateral ventricle, the actual midline usually splits the left and right lateral ventricles. For a CT slice in which the left and right lateral ventricles can be distinguished and can be separated very clearly, a simple approach to estimate the midline is to project the region containing the lateral ventricles in one direction and to identify the splitting point by minimizing the number of pixels on one projection. This method may work well if it is fed with very well segmented regions, with very little noise or mis-segmentation. However, this is often not the case in the brain CT scans, as illustrated in Figure 6.1.

The method proposed in this thesis follows a computer vision approach using shape matching. Since the result of the ventricle segmentation is a binary image (ventricle regions as object and non-ventricle regions as background), all that can be seen in such a binary image is the shape information. In order to identify different regions of the ventricle and estimate the actual midline, a mapping can be built between the segmented shape

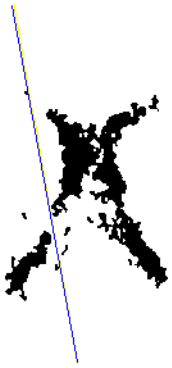

Figure 6.1: The wrong estimation of actual midline (straight line in the figure) based on minimal cut.

and a standard ventricle template with annotated information. For instance, considering the bilateral ventricle slice, if the edge points in the middle on the left and right lateral ventricles are detected, a midline can be estimated that separates the left and right side. The approach in this thesis seeks to match/register ventricle templates with the segmented ventricle shapes in order to identify the feature points from point correspondences between the shapes.

Shape matching is a fundamental problem in computer vision. Based on the shape representation, shape matching methods can be divided into two types: feature-based methods and intensity-based methods. The first method extracts silhouette images from the shape, which do not have holes or internal markings. Fourier descriptors can be used to capture the curve information, e.g. [104] [73]. A comprehensive comparison of different silhouettes based methods is given in [45]. Other feature based representation methods are based on graph structure, including skeleton [88] and shock graph [86]. The limitation of the silhouette-based method is that it ignores internal structure, leading to loss of some important information. Another problem is that silhouettes are not easy to

extract. Recently a wavelet based method has been developed to extract density from shape points, showing promising results [74]. The second group, intensity-based methods, use the gray/color image directly. Cootes [16] applies a statistical model to iteratively match points based on intensity value. This gives correspondence between the model and the points on images. Other intensity based methods use classifiers to classify different shapes [68]. Since one needs explicit correspondence to derive feature points after ventricle segmentation, these methods are not considered in this research. The method in [4] uses simple sampling of shape, introducing shape context descriptor to represent shapes. This method is very effective and robust, and is therefore adopted for ventricle shape matching and midline estimation.

6.2 Actual Midline Estimation

6.2.1 Specifying Feature Points

The first challenge is how to define an actual midline from a CT scan. In general, the actual midline should separate two lateral ventricles and pass through the middle of the third ventricle. However, in order to identify the midline automatically, this definition must be made more specific. Since ventricular shapes are irregular, due to variations among different people and considering different pressure levels inside the brain, it is not easy to find a simple mathematical method to define the midline. The approach proposed in this thesis first identifies some feature points on the shape, e.g., the edge points between the bilateral ventricles, and then uses these points to estimate the midline. Because the shape of the third ventricle is entirely different from the bilateral ventricles, feature points for different CT slices need to be specified for individual slices. Figure 6.2 shows the templates with feature points, which are manually labeled. For each template shape, feature points

on the left side and right side are specified with a brighter color. Considering the fact that in some pathological cases some ventricular regions may be absent or be fused together, another 8 template variations representing these pathological cases were formed and added to the list of template used for different slices. Figure 6.3 shows the extra templates. All of these templates are formed from MR images that allow a more accurate imaging of the ventricles and their locations. Based on the slice location in the CT scan and MRI, a coarse mapping between the CT slice and templates are estimated. For each CT slice, besides the coarse matched template slice, 4 superior and inferior template slices are also included as matching candidates.

6.2.2 Shape Matching Between Templates and Segmented Ventricles

For shape matching, a modified version of the shape context method [4] is adopted. This is used because it is a point-based shape matching approach. This is more suitable than curve or contour based methods, which are too strict in assuming that all segmented shapes form a single connected curve or contour. It is not simple or sometimes even possible to extract the exact curves or contours of ventricles needed from the CT slices. For point based shape matching, only point sampling from the desired shape is required. Also, the shape context method is very robust to deformation, outliers and noise, which is very important in particular for slightly pathological cases processed using ventricle templates representing normal brains.

Here a simple description of the modified version of shape matching using shape context, proposed by this research is given; other details about the shape context can be found in [4]. First, shapes are sampled uniformly, usually by taking edge points because these points represent the shape better than other points such as points inside solid areas. In

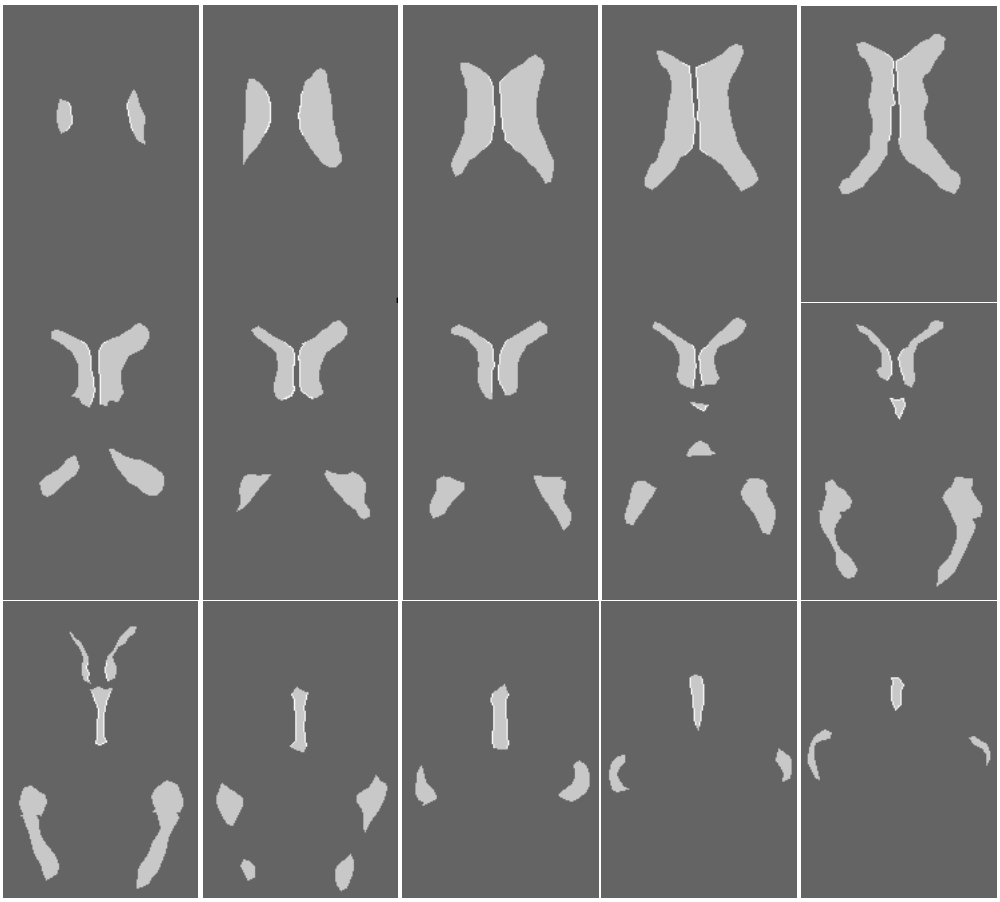

Figure 6.2: 15 ventricle templates from MR images.

addition, dummy points can be added that not only make the number of matching points equal but also allow outlier matching in two shapes. The shape context is a descriptor used for each point in the sampled shape. It views all other points from its position and computes the histogram of the distribution. The histogram binning is uniform in log-polar space, which emphasizes the points close to the center points. Figure 6.4 shows an example of formation of such a histogram[1].

After computing all the shape context descriptors, a matching cost is defined for a

[1]This figure is inspired by [4]

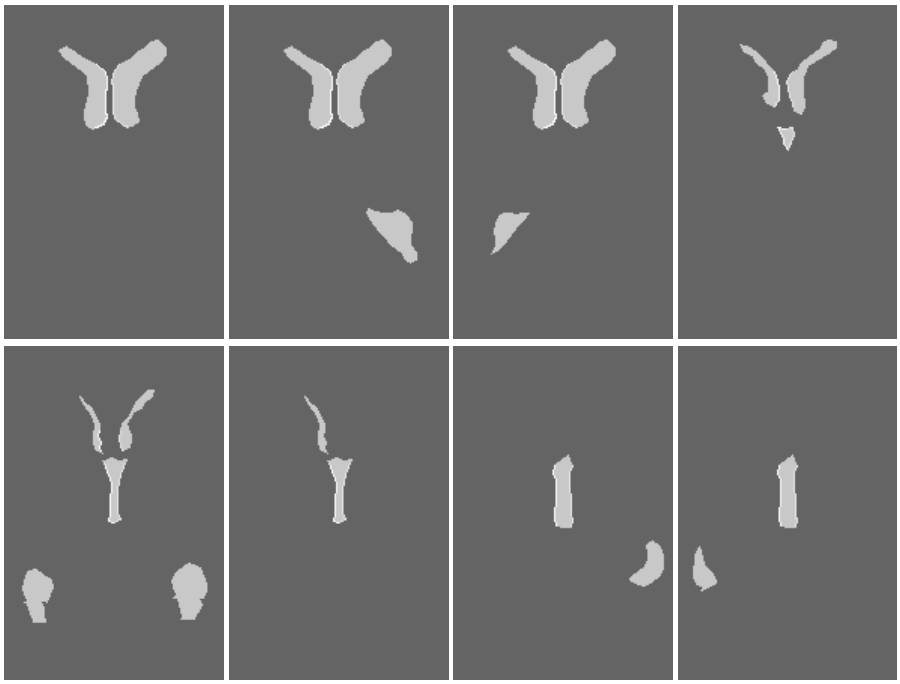

Figure 6.3: 8 extra variations of ventricle templates.

point p_i on the first shape and q_j on the second shape, as follows:

$$C_{ij} \equiv C(p_i, q_j) = \frac{1}{2} \sum_{k=1}^{K} \frac{[h_i(k) - h_j(k)]^2}{h_i(k) + h_j(k)}, \tag{33}$$

where $h_i(k)$ and $h_j(k)$ denote the K-bin normalized histograms at p_i and q_j, respectively. Then the shape matching can be achieved by minimizing the following cost function:

$$H(\pi) = \sum_i C(p_i, q_{\pi(i)}), \tag{34}$$

subject to the constraint that the matching be one-to-one, i.e., π is a permutation. The permutation function π can be defined as a mapping from one arrangement to the other arrangement such as $\pi : S \rightarrow S$, where S is the set of $1, 2, \cdots, n$. This is an bipartite graph matching problem which can be solved by the Hungarian method [70]. The next step is modeling the transformations using the thin plate spline (TPS) model [21] [62],

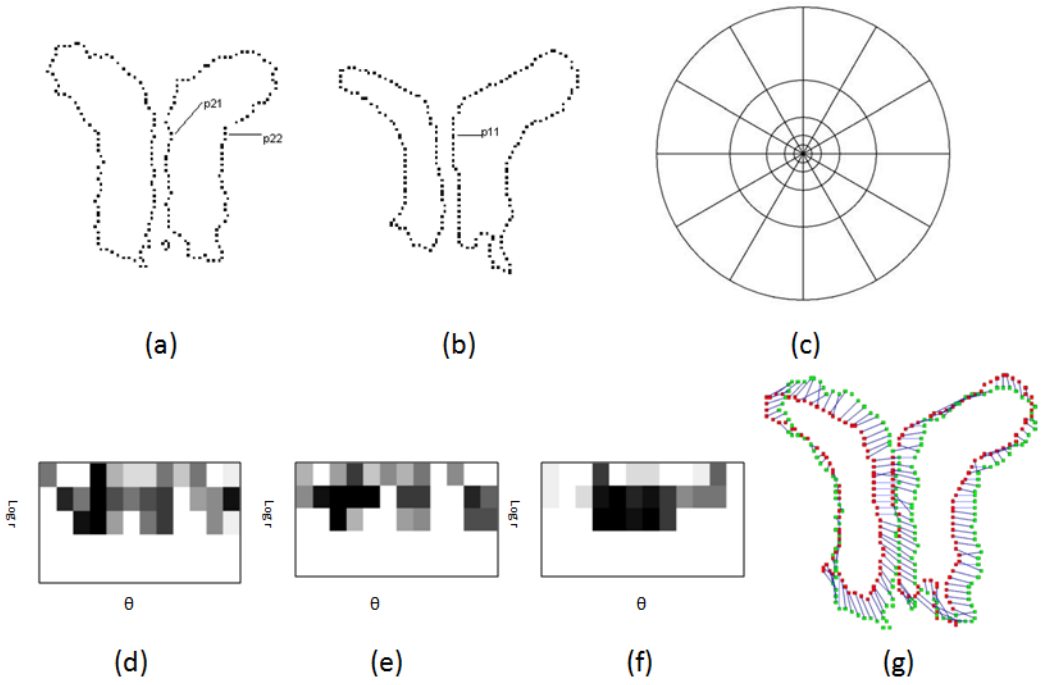

Figure 6.4: (a) and (b) are the sampled edge points of the two shapes. (c) is the diagram of the log-polar bins used to compute the shape context. (d) is the shape context for the point p21, (e) is that of point p11, and (f) is that of point p22. (d) and (e) are the shape contexts for two closely related points which are similar (this can be seen from the white gaps in both images). However, the shape context in (f) is very different from the previous two. The shape context matrix colormap for the images is inverted before displaying.

which is a commonly used nonlinear transformation. The coordinate transformation is modeled using two separate TPS functions, i.e., $f_x(x, y)$ and $f_y(x, y)$.

$$(x^{'}, y^{'}) = T(x, y) = (f_x(x, y), f_y(x, y)). \tag{35}$$

The $f_x(x, y)$ or $f_y(x, y)$ has the form:

$$f(x, y) = a_1 + a_x x + a_y y + \sum_{i=1}^{n} w_i U(||(x_i, y_i) - (x, y)||), \tag{36}$$

where the kernel function $U(r)$ is defined by $U(r) = r^2 log r^2$ and $U(0) = 0$ as usual. a_1, a_x, a_y, w_i are the coefficients to be estimated given a set of corresponding points (x_i, y_i)

from the first shape and $(x_i^{'}, y_i^{'})$ from the second shape. The TPS transformation and shape context matching iterates several times to optimize the mapping. Bending energy can also be used as the component for calculating the similarity of two shapes [4]. The motivation for using transformation modeling is that overly-complex transformations can be penalized using regularized TPS. In addition, this method is used to generalize the point correspondence to any point in the space.

In this thesis, only the cost function of shape matching is used to measure the similarity between segmented ventricle shapes and templates, and TPS modeling is not used. The reason for not using TPS modeling is that even though TPS iteration can adjust some mis-matching points, it does not improve the results too much if the mis-matched points are too far away from the points that should be matched.

6.2.3 Challenges in Ventricle Shape Matching for Pathological Cases

In pathological cases, different ventricular parts may shift away from each other or move closer; this changes the relative positions of these parts. For example, the distance between the left and right lateral ventricles in pathological CT scans may be bigger than that in of templates. This will change the histogram of each sampled point and make the shape matching with template a challenging task. The second common issue is that different ventricular parts may change their size in different scale. For example, in some CT slices, while the left lateral ventricle shrinks, the right ventricle expands. If the point sampling process is uniform, this will result in the shrinking part being underrepresented (i.e., fewer sampling points are sampled from this part). On the other hand, the sampled template shape assumes the same scale on both lateral ventricles and has close number of sampling points for both sides. This sampling inconsistency of matching regions (parts) may cause

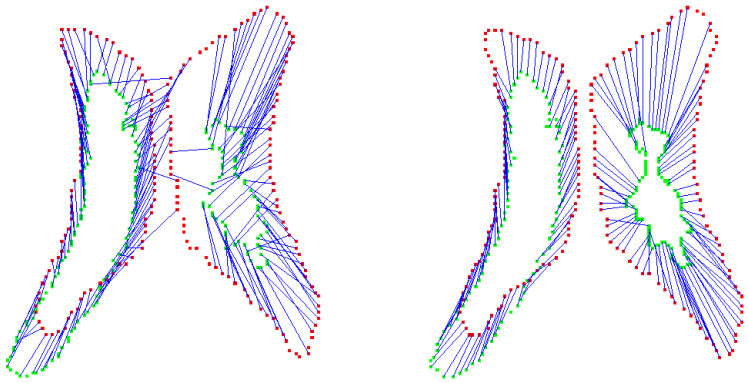

(a) (b)

Figure 6.5: Comparison of simple shape matching and multiple regions shape matching.

superfluous points of one region matched to the other regions. While these two problems can not be fixed by global rigid registration because the deformation is not global, a local deformation may be alleviated by local non-rigid deformation [35]. In this thesis, these problems are addressed in a multiple regions shape matching scheme. Figure 6.5 shows the problem of entire shape matching as well as the result of the proposed method. Figure 5(a) is the result of shape matching with the entire shapes, which exhibits the mis-matching points between left and right sides. Figure 5(b) is the result of multiple regions shape matching. The template is in red and the segmented ventricles in green. The blue lines represent the correspondences.

6.2.4 Multiple Regions Shape Matching

The main idea is that first a shape matching is done with all regions between the segmented ventricle shape and the template. Then the corresponding regions of the two shapes are estimated and grouped into several sets based on the initial matching result. For each set of corresponding regions from the two shapes, points are sampled and shape matching is

performed again. The algorithm is further described using the following example. Consider two shapes A and B. Shape A has three regions A_1, A_2 and A_3, while B has four regions B_1, B_2, B_3 and B_4. Both shapes A and B are sampled with uniform sampling, upon which a shape matching is done between them. After the initial match, based on the estimation from the point correspondence, suppose A_1 is matched to B_1, B_2, A_2 is matched to B_3, and A_3 is matched to B_3, B_4, which in total forms three matching sets. For each set, e.g., A_1, B_1, B_2, sampling is performed again to obtain the same sample points from A_1 and B_1, B_2, then shape matching is performed inside the set without considering other regions. This means that all shape contexts are calculated using only shape regions inside the set. This multiple regions shape matching scheme can deal with the problems explained previously assuming the correct estimation of matching regions sets. In the second shape matching, since other non-matched regions are not considered in the histogram calculation, the location changes of these regions will not influence the shape matching inside the matched regions set. Because of the resampling in the second shape matching, shrinking regions will have the same number of points represented in the matching process. The multiple regions shape matching scheme is listed in Algorithm 1.

Algorithm 1 Multiple Regions Shape Matching

```
1: Entire shapes sampling and initial shape matching
2: Group matched regions into several matching sets
3: for each matching set do
4:     Resample these regions to have the same points from each shape
5:     Do shape matching with these points
6: end for
7: Put all matching points together and calculate the total matching cost
```

There are still two questions to be answered: how to estimate the matching regions and how to calculate the matching cost from several matching regions. For the first question,

note that each pair of corresponding points is associated with a matching cost. Using a threshold on the matching cost, 30 percentile in the application, the most reliable correspondences can be selected. Applying a statistical analysis of the selected correspondence, regions can be grouped into different sets. The detailed steps are listed in Algorithm 2.

Algorithm 2 Group Matched Regions

1: Set a cost threshold to select reliable matches
2: **for** each region A_i in the first shape A **do**
3: Calculate the average number of matched points n_i from A_i to regions in shape B
4: Any region B_j has more than $0.5 * n_i$ matched points to A_i are related with A_i
5: **end for**
6: Do the same process on the second shape B to build regions relation with shape A
7: The shape regions that are related directly or indirectly through other regions form a set of matched regions

The total matching cost of the two entire shapes is calculated based on each matching set. First the matching cost of each set calculated from 34 is normalized by the number of sampling points. In order to give more weights to the matching cost of the larger regions, the total matching cost is the weighted average of the costs for matching regions based on region area, which can be the sum of areas from the matching regions. Figure 6.6 shows the top 3 matching costs between the templates and the segmented ventricle shape. The segmented ventricle is in green, the template in red and correspondence in blue.

6.2.5 Estimation of the Actual Midline

Based on the identified feature points on the ventricle shape from shape matching, the actual midline can be estimated. Since the feature points are labeled as left side and right side, a simple way is to use the average of left side mean and right side mean of the x-coordinates to define the x-coordinate of the midline. This simple estimation method is used here, however more sophisticated estimation method can be applied to

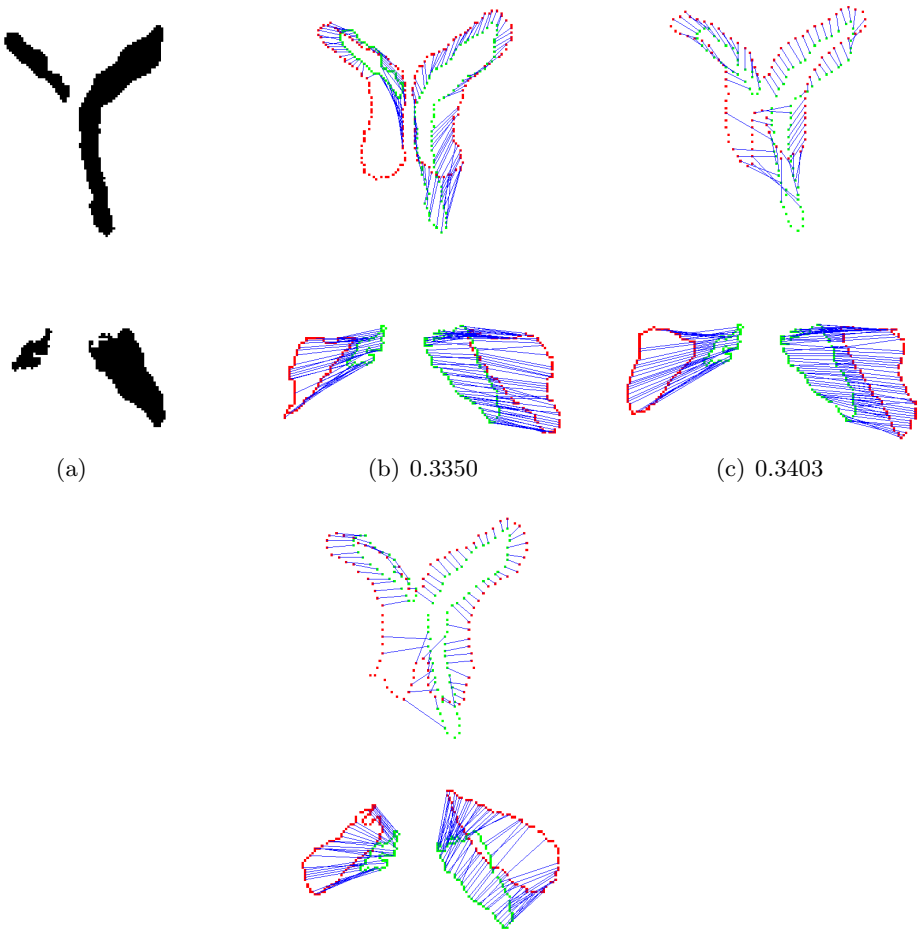

(a) (b) 0.3350 (c) 0.3403

(d) 0.3419

Figure 6.6: Segmented ventricles are matched with 3 templates.

further improve the method. Figure 6.7 shows several estimated actual midline for different ventricle slices. The green lines are the estimated actual midlines and the blue dots represent the best matched template. Matched feature points on the left side are in red and right side in a darker red. As it can be seen, the actual midlines are successfully estimated by the identified feature points.

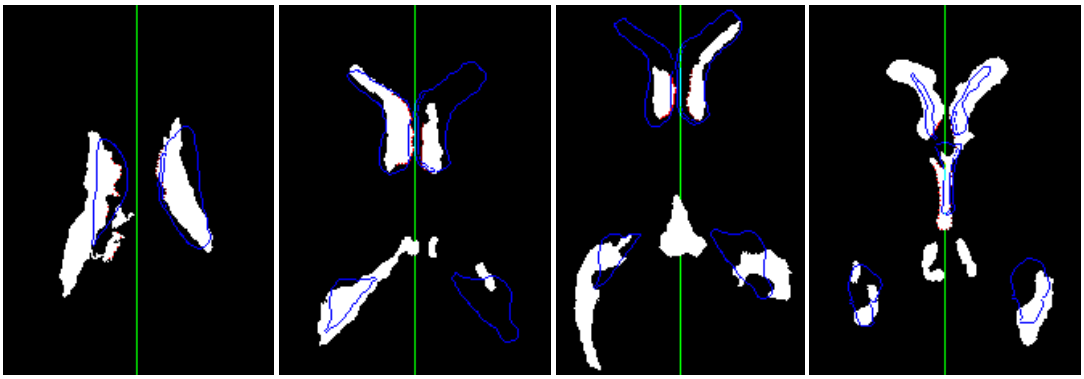

Figure 6.7: The actual midline estmation results.

6.3 Results

6.3.1 Data

The testing CT dataset was provided by the Carolinas Healthcare System (CHS). All subjects were diagnosed with mild to severe TBI when first admitted to hospital. The dataset contains 40 patients. From this set, 391 axial CT scan slices are selected that show ventricles or region that should have contained ventricles. To our knowledge, and based on the literature of the brain CT image processing [46] [78] [103], our database is relatively large, and as a result, the reliability of the testing results for the proposed CT segmentation method should be at least as high as that of almost all comparable works in this field.

6.3.2 Evaluation of Actual Midline Estimation

The same dataset is used for testing actual midline detection as for ventricles segmentation. Some of the 391 CT slices cannot be processed by the proposed method. Specifically, there are three classes for these non-applicable images. The first includes images in which no ventricle falls inside the template. The second category includes images where ventricles

segmentation has been done inaccurately. This often happens in segmentation results that include edema which are very close to the ventricles. The third class occurs when one or both of the lateral ventricles are completely missing in the images. In such cases, ventricle segmentation result cannot be used even by a human expert to draw the actual midline. After a Gaussian Mixture Model (GMM) based segmentation process [13], manual drawing of the midline in ventricle area on the segmentation result is done by participating radiologists. The slices in which one side of the lateral ventricle is missing or the ventricles are not visible are not applicable for visual inspection and thus excluded. As such, 264 manually tagged slices are collected and used.

Since almost all manually tagged midlines are either in the exact vertical direction or tilted with a very small angle, the quality of the estimated midline is evaluated based on the aggregated x-coordinate, which is the average x-coordinates of all points on the actual midline. The resolution of CT images is $512 * 512$, with the pixel spacing of 0.4492 mm. We specify 5 pixels as the tolerance threshold, which is equivalent to 2.25 mm in real physical dimension. This threshold seems reasonable because in diagnostic applications, midline shift greater than 5 mm is thought of as serious and needs to be taken care of. With this threshold, the success rate of our method is 87.9% (232/264). The mean value of the error is 1.23 pixels and the standard deviation is 1.34 pixels among the successful slices. This is very promising considering that all processed images are pathological CT slices from TBI patients. Figure 6.7 presents some images for actual midline detection.

After the actual midline is estimated, the calculation of the horizontal midline shift s is straightforward:

$$s = |x_{ideal} - x_{est}| \tag{37}$$

where x_{ideal} is the x coordinate of the ideal midline, and x_{est} is the x coordinate of the estimated actual midline. Figure 6.8 shows both the ideal midline and estimated midline.

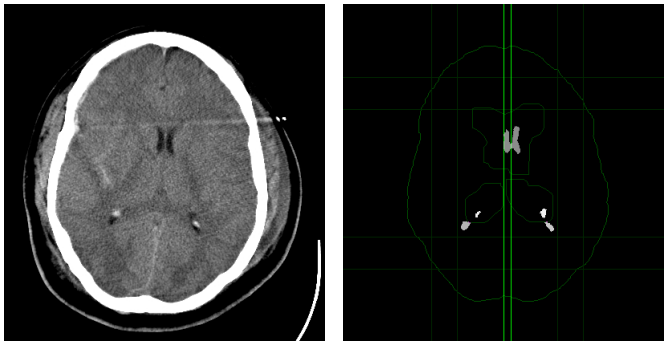

(a) Original CT image (b) Midline shift estimation

Figure 6.8: The left line is the ideal midline and right line is the estimated actual midline.

6.4 Conclusion

As supported by experiments, the proposed multiple regions shape matching method addresses the problem in shape matching of deformable and complex structures. The actual midline estimation shows very robust performance on diverse ventricle shapes, which is vital for pathological cases. Because the algorithm follows a computer vision approach, it handles the variations in different segmented ventricle shapes in a intuitive and effective way using a few ventricle templates.

CHAPTER 7 Application: Intracranial Pressure (ICP) Prediction

7.1 Introduction

Elevated Intracranial Pressure (ICP), is a very common secondary injury in TBI that if not treated in time can result to potentially deadly consequences such as ischemia or herniation. A standard and accurate method of monitoring ICP is inserting pressure sensors inside ventricles through a brain surgery, which may cause infection and both short-term and long-term damages to the brain. Due to the invasive nature of this monitoring system, non-intrusive screening/pre-screening of ICP is highly desirable even though such screening process may not be as accurate as the intrusive surgery. Rather, the non-surgical ICP estimation can serve as pre-screening procedures to assist care-giver in making decision on whether or not an intrusive monitoring is necessary. CT scan is one of the main sources of diagnostic information in exploring the brain state in TBI care. The reason for choosing CT scan instead of other imaging modalities, such as MRI, is that CT scan is still the gold standard for initial TBI assessment [63]. Moreover, CT has the advantage of revealing hematoma or bone fracture with reasonable resolution. CT also has low cost and fast scan speed. In the application described in this chapter, multiple non-intrusive sources of measurement are collected and analyzed in order to extract informative features with respect to the range of ICP; then a classification model is built that considers these features to predict the level of ICP.

7.2 Features Extraction

Hematoma and edema are two common pathological features in traumatic brain injury, e.g., in the case of brain contusion, these two are the main factors. Because of the swelling effect from hematoma or edema, the brain structure may shift to the opposite side of the location of swelling. The midline (the intersection between the fissure separating the two hemisphere and the axial plane) often shift from the middle to one side. This midline shift will be measured as a possible feature for predicting ICP level. Another useful feature is the blood amount due to hematoma or hemorrhage. The bleeding area may push other brain tissues to the side and increase the pressure inside the brain. The third set of features investigated is the texture patterns of the brain tissue. Because of high pressure inside the brain, the texture of both the gray matter and the white matter may change, e.g., these brain tissues get denser than normal state. All these three sets of features are extracted from brain CT scans. Specifically, all these features are extracted from each CT scan slice, and then aggregated by combining the same type of features from multiple slices in a CT scan as feature representing the entire CT scan. Besides these features extracted from the CT scan, demographic information, such as patient age, and medical score, such as Injury Severity Score (ISS) are also included. These features may also provide extra information to the model of predicting the ICP level. In the following sections of this chapter, the extraction of each set of features are described in more detail.

7.2.1 Midline Shift

The midline shift measurement is one of the most characteristic feature of ICP elevation. The shift for every CT slice is estimated using the techniques described in the previous

chapters.

7.2.2 Blood Amount

The measurement of blood amount is based on the Gaussian Mixture Model (GMM) segmentation result of the CT slices, because the segmented CT slices have already classified each pixels into four categories: blood, ventricles, gray matter and white matter [13]. Figure 7.1 shows the segmented result from GMM segmentation. By counting the number of pixels classified as blood for each slice and summing them up, a feature as the total number of blood pixels is formed that quantifies the blood amount.

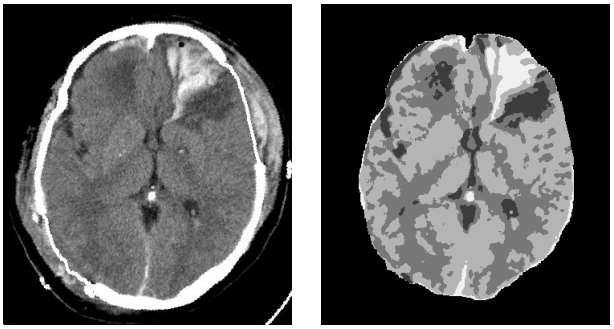

(a) Original CT image (b) GMM segmentation map

Figure 7.1: The GMM segmentation result of the brain. The blood regions are represented as the brightest gray level in the segmentation map.

7.2.3 Texture Pattern

CT imaging does not provide a high resolution for the brain tissue as MRI does, and as such it cannot differentiate dozens of brain structures clearly; in the CT slices the brain structures are not clearly separated and represented. However, some regularity or pattern, even though scattered, may still be present inside the CT slices that although hidden to human eye can be processed and used for ICP prediction by effective mathematical

algorithms. One possible pattern/regularity may be that with the increase of ICP, the density of the brain tissue increases because of the compression, which may result in the change in the appearance/texture of the CT images. Such possible patterns motivate the texture analysis on the CT images for ICP prediction. For each CT slice, six rectangular sub-images (windows) are selected to contain the brain tissue in that region while avoiding blood and ventricles regions. Several different types of texture analysis can be applied in this application [38] [1]. Here a brief description of the main techniques for extraction of texture features used in this research are provided.

The first set of texture features is generated using histogram with 10 bins. The mean, variance of the histogram are extracted as texture features. A smoothness feature $R = 1 - 1/(1 + \sigma^2)$ which is a function of variance σ^2 is also calculated as a texture feature. The fourth feature is the variance of the image region.

The second set of texture features is generated using Grey Level Run Length Method (GLRLM) [97][82][23], which extracts higher order statistics of the texture using a matrix $R(\theta) = [r(i, j|\theta)]$. The element $r(i, j|\theta)$ is the number of consecutive runs of length j at gray level i in the direction θ. In this application, 0, 45, 90 and 135 degrees are used for θ. By using different weighting scheme, 11 features can be extracted from the matrix to represent the regularity and periodicity of the image.

The third set of texture features is generated using Discrete Fourier Transform (DFT). After the DFT of the sub-image is calculated, the maximal, minimal, median and mean value of the amplitude of DFT, as well as the frequency corresponding to the median value of amplitude of DFT are extracted as the texture features.

The fourth set of texture features is generated using wavelet packet transformation.

First the image region is decomposed into the second level with Haar wavelet. This generates 16 images on the second level. Then the energy of each image is calculated as texture features. The last feature is the entropy calculated using the energy features.

The fifth set of texture features is generated using Dual Tree Complex Wavelet Transform (DTCWT) [42] [87]. Dual tree complex wavelet transform is designed to overcome some shortcomings when applying Discrete Wavelet Transform (DWT) in higher dimension (e.g., image processing), such as oscillations, shift variance and lack of directionality. In image processing applications, this method is known to be free of checker board artifact and to provide 6 directional wavelets. In this application, the entropies calculated from coefficients of the lowpass sub-band and the highpass sub-band of each level are used as texture features.

Overall, 48 texture features are collected for each sub-image region and then averaged across the six sub-images.

7.2.4 Demographic Information and Injury Score

Ages of each patient is considered as the main demographic information. Injury Severity Score (ISS) as the main measure of traumatic injuries is also selected as a feature.

7.2.5 Feature Aggregation across CT Slices

Since all the image processing features are extracted slice by slice, they need to be organized to represent the state of the entire CT scan and then be comparable among different patients. One approach to do this is to organize the features by location. This requires slice alignment/registration among all CT scans. Since the slice thickness between the CT slices is often large, i.e., over 10 times bigger than the pixel dimension inside the slice, even

perfect registration of CT slices among patients would bring a relatively large alignment errors in the order of the slice thickness. Hematoma and edema among patients further complicate the registration process. Yet another reason that registration may not be necessary is that the location of injury inside the brain may be different among patients. All these suggest that the alignment with the injury location, e.g., the comparison of the texture patterns around the injured regions, may provide a better solution for ICP prediction.

In order to aggregate of extracted features, a statistical approach is taken with the assumption that the procedure can reveal the critical information needed for ICP prediction from calculated features. Statistics of features across slices are calculated and used to represent the features of an entire CT scan. Specifically, $min(f)$, $max(f)$, $median(f)$, $mean(f)$, $std(f)$ are calculated for a feature f from the midline shift feature set or the texture feature set. For the blood amount feature, besides the 5 operators listed above, $sum(f)$ is also added to record the total blood volume.

7.3 Data

7.3.1 Data Preparation

The collected data includes 17 patients with mild to severe TBIs, which were provided by the Carolinas Healthcare System (CHS). The age ranges from 8 to 70.1, with mean value 38.4 and standard deviation 19.2. Each patient has several CT scans. Some have surgeries performed between two consecutive CT scans. Therefore, in total, 56 CT scans were used for this study. With each CT scan, CT slices that show ventricles or regions that should have contained ventricles were selected for image analysis because these regions contain the features explained above. Usually 5 slices from each CT scan are selected in this

process.

7.3.2 ICP Level Labeling and Prediction

For each patient, the ICP value is recorded every hour at any given day. To associate the ICP value with each CT scan, the two closest measurements of ICP to the time of CT scan acquisition (both within an hour) are averaged and assigned as the ICP value at the time of the CT scan. Then the ICP values are grouped into two classes: elevated ICP with ICP$>$ 15 and normal ICP with ICP$\leq$ 15. With this ICP level thresholding, there are 31 cases of normal and 25 cases of elevated ICP.

7.4 Feature Selection

Overall, 274 features are extracted. Since there are only 56 cases, feature selection is performed to reduce the feature space and select only the most relevant features to improve generalization ability. Feature selection methods can be grouped into two categories [43] [44]. The first category is called a filter that usually considers the relationship between features and target using some defined conditions, such as correlation, directly. The second category is called a wrapper which incorporates a classifier and selects features based on the classification accuracy. The feature selection methods in the first category are much faster than the methods in the second category, however, methods in the second category usually produce higher classification accuracy. A common practice to select features from a large set of candidates is performed in two stages [72]. In the first stage a filter-like feature selection method is used to rank all features. Then a small number of top ranked features is selected as the refined candidate sets. In the second stage, a wrapper of feature selection method is employed to select a feature set with high testing accuracy. In this

thesis this feature selection scheme is applied. The ReliefF algorithm [81] is applied in the first stage to select the top 40 features. Since midline shift, blood amount, demographic information and ISS may provide useful information for ICP prediction in the medical point of view, these features are also added because some of these features are not in the top 40 rank list. In total, 52 features are selected for further process.

In the second stage, the Support Vector Machine (SVM) is used in the wrapper for the classification of feature set. In the validation step, the 10 fold cross-validation result is used as the accuracy measurement. Radical Basis Function (RBF) kernel is used with fixed parameters of $C = 32768$ and $\gamma = 0.125$. The search method used to construct feature set is Best First [43]. Since the midline shift, blood amount and ISS are very relevant to ICP, these 3 features are set as the initial set of the search set. The feature subset achieving the best validation accuracy for ICP prediction is selected as the final feature set. Table 7.1 shows the final selected feature set. All the feature selection and classification experiments are performed in Weka [30].

Table 7.1: Selected Features

max(midline shift)
max(normalized midline shift)
median(normalized midline shift)
ISS
sum(BloodCount)
One std(FFT feature)
One std(DWCWT feature)
Two min(Wavelet feature)
One mean(Wavelet feature)
One max(Variance feature)
One std(Wavelet feature)
One median(GLRLM feature)

7.5 Classification Result

After the feature selection step, 10 fold cross validation were performed 10 times with random split of the data. Table 7.2 shows the mean value as well as standard deviation of the classification results in percentage. As it can be seen, the classification accuracy is

Table 7.2: Classification Result

Sensitivity	Specificity	Accuracy
84.83 ± 3.43	80.40 ± 6.38	82.86 ± 4.05

promising in predicting ICP levels. This also verifies the usefulness of selected features for ICP prediction.

7.6 Conclusion

In this application, an ICP level prediction method is proposed and validated using machine learning method. Multiple sources of features are used, including automatically calculated midline shift, texture patterns and blood amount extracted from the brain CT images. Other features such as age, ISS are also considered. Selecting informative features from the original feature set provides a promising ICP prediction model is built, which is validated using machine learning algorithm. Future work may include further investigation of the medical interpretations of the selected features and further evaluation the method on larger datasets.

CHAPTER 8 Conclusion and Future Work

8.1 Conclusion

This thesis provides a framework for automated midline shift detection in axial head CT images. First, an accurate ideal midline detection method is proposed and then CT scan images are aligned to the ideal midline. The ventricles are then recognized via initial spatial segmentation followed by template matching using templates extracted from an axial head MRI scan. Finally, using multiple regions shape matching method the actual midline is drawn and the horizontal midline shift is calculated. The proposed method offers the following improvements over existing approaches: accurate detection of ideal midline, the use of both anatomical features and spatial templates derived from MRI images to identify ventricles from pathological CT images, and a multiple regions shape matching algorithm which provides a very robust actual midline drawing method to deal with diverse ventricle shapes. Moreover, the relatively large size of the CT dataset used for testing makes the results of this study more reliable. This thesis also provides a general framework for automated midline shift measurement. Because of the separation of steps, each part can be designed and improved almost individually, which facilitate the development of the entire system. Another advantage of the thesis is that the results of each step can be further improved with the improvement made to the previous steps.

The study also intends to predict ICP based on features extracted from CT images, including midline shift, texture feature and features from demographical information. The

prediction results using machine learning method are promising. This also indicates that the proposed automated midline shift measurement is accurate enough for practical application.

8.2 Future Work

In the proposed segmentation, the low level segmentation and high level recognition are separated and currently there is no feedback from the high level to the low level segmentation. This is different from human visual inspection, which has interactions between low level vision and high level recognition. One possible approach to combine these together is "model based low-level segmentation". In this method, the low-level segmentation may be guided by high level atlas models of the target structure.

For the actual midline estimation, a imaginary line is estimated to draw the actual midline. This emulates the approach used when experts draw the midline manually. However, it is observed that in addition to horizontal shift, there is often twisting in ventricle regions, i.e., the midline is not always vertical. This requires an additional algorithmic process to calculate the deformation of the angle of the midline. Other useful information about the midline shift includes the deformation in the upper part and lower part of the brain, besides the shift along the ventricles. Future work will therefore include detection of midline deformation in these regions. This requires other features to be extracted to estimate the actual midline in the corresponding regions.

Future work will also focus on extraction of other features, such as more details about the ventricle to predict the ICP value. For instance, the asymmetry of the lateral ventricles may indicate an unbalanced increase in ICP. Also more data are needed for ICP prediction

to further verify the proposed model.

Bibliography

Bibliography

[1] A. Todd-Pokropek AE Svolos. Time and space results of dynamic texture feature extraction in mr and ct image analysis. *IEEE Trans Inf Technol Biomed*, 2(2):48–54, 1998.

[2] E. Bak and K. Najarian. Domain conversion with local posteriors for image segmentation. In *Proc. IEEE International Conference on Acoustics, Speech, and Signal Processing (ICASSP'04)*, pages 745–748, Montreal, Quebec, May 2004.

[3] EunSang Bak and Kayvan Najarian. Robust segmentation using parametric and nonparametric local spatial posteriors. In *Proceedings of the International Conference on Information Technology: Coding and Computing (ITCC2004)*, 2004.

[4] S. Belongie, J. Malik, and J. Puzicha. Shape matching and object recognition using shape contexts. *IEEE Trans. Pattern Anal. Mach. Intell.*, 24(4):509–522, 2002.

[5] Marie-Odile Berger. Snake growing. In *Proceedings of the First European Conference on Computer Vision*, pages 570–572, 1990.

[6] J. Besag. On the statistical analysis of dirty pictures. *J. R. Statist. Soc, B*, 48(3):259–302, 1986.

[7] J. Besag. On the statistical analysis of dirty pictures. *J. R. Statist. Soc, B*, 48(3):259–302, 1986.

[8] J. C. Bezdek, L.O.Hall, and L.P.Clarke. Review of mr image segmentation techniques using pattern recognition. *Med. Phys.*, 20(4):1033–1048, July 1993.

[9] M. E. Brummer. Hough transform detection of the longitudinal fissure in tomographic head images. *Medical Imaging, IEEE Transactions on*, 10:74–81, 1991.

[10] Chad Carson, Serge Belongie, Hayit Greenspan, and Jitendra Malik. Blobworld: Image segmentation using expectation-maximization and its application to image querying. *IEEE Transactions on Pattern Analysis and Machine Intelligence*, 24:1026–1038, 2002.

[11] Arthur Chan, Jahanzeb Sherwani, Ravishankar Mosur, and Alex Rudnicky. Four-layer categorization scheme of fast gmm computation techniques in large vocabulary continuous speech recognition systems. In *Proceedings of INTERSPEECH 2004*, pages 689–692, 2004.

[12] Chih-Chung Chang and Chih-Jen Lin. *LIBSVM: a library for support vector machines*, 2001. Software available at http://www.csie.ntu.edu.tw/ cjlin/libsvm.

[13] Wenan Chen and Kayvan Najarian. Segmentation of Ventricles in Brain CT Images Using Gaussian Mixture Model Method. In *Proceedings of IEEE International Conference on Complex Medical Engineering*, pages 15–20, April 2009.

[14] Wenan Chen, Rebecca Smith, Soo-Yeon Ji, and Kayvan Najarian. Automated segmentation of lateral ventricles in brain ct images. In *Bioinformatics and Biomeidcine Workshops, 2008. BIBMW 2008. IEEE International Conference on*, pages 48–55, 2008.

[15] Wenan Chen, Rebecca Smith, Soo-Yeon Ji, Kevin Ward, and Kayvan Najarian. Automated Ventricular Systems Segmentation in Brain CT Images by Combining Low-level Segmentation and High-level Template Matching. *BMC Medical Informatics and Decision Making*, 9 Suppl 1, 2009.

[16] D.H. Cooper, T.F. Cootes, C.J. Taylor, and J. Graham. Active shape models - their training and application. *Computer Vision and Image Understanding*, pages 38–59, 1995.

[17] T.F. Cootes, A.H. Hill, C.J. Taylor, and J. Haslam. The use of active models for locating structures in medical images. *Image and Vision Computing*, 12(6):355–366, 1994.

[18] Chris A. Davatzikos and Jerry L. Prince. An active contour model for mapping the cortex. *IEEE TRANSACTIONS ON MEDICAL IMAGING*, 14(1):65–80, 1995.

[19] A. P. Dempster, N. M. Laird, and D. B. Rdin. Maximum likelihood from incomplete data via the em algorithm. *Journal of the Royal Statistical Society, Series B*, 39:1–38, 1977.

[20] F. Ding, W. K. Leow, and S.-C. Wang. Segmentation of 3d ct volume images using a single 2d atlas. In *First International Workshop on Computer Vision for Biomedical Image Applications (CVBIA 2005)*, pages 459–468. Springer Berlin / Heidelberg, 2005.

[21] Jean Duchon. Splines minimizing rotation-invariant semi-norms in sobolev spaces. In W. Schempp and K. Zeller, editors, *Constructive Theory of Functions of Several Variables*, pages 85–100, Berlin, 1977. Springer.

[22] B. Fischl et al. Whole brain segmentation automated labeling of neuroanatomical structures in the human brain. *Neuron*, 33(3):341–355, 2002.

[23] M.M. Galloway. Texture analysis using grey level run length. *Computer Graphics Image Processing*, 4:172–179, 1975.

[24] G.B.Coleman and H.C. Andrews. Image segmentation by clustering. *Proceedings of the IEEE*, 67(5):773–785, May 1979.

[25] D. Geiger and F. Girosi. Parallel and deterministic algorithms from mrfs: surface-reconstruction. *Pattern Analysis and Machine Intelligence, IEEE Transactions on*, 13(5):401–412, 1991.

[26] Stuart Geman and Donald Geman. Stochastic relaxation, gibbs distributions, and the bayesian restoration of images. *IEEE Transactions on Pattern Analysis and Machine Intelligence*, 6(6):721–741, Nov 1984.

[27] Rafael C. Gonzalez and Richard E. Woods. *Digital Image Processing*. Prentice Hall, 2 edition, 2002.

[28] V. Grau et al. Improved watershed transform for medical image segmentation using prior information. *IEEE Trans. Med. Imag.*, 23(4):447–458, 2004.

[29] Hayit Greenspan, Amit Ruf, and Jacob Goldberger. Constrained gaussian mixture model framework for automatic segmentation of mr brain images. *IEEE Trans. Med. Imaging*, 25(9):1233–1245, 2006.

[30] Mark Hall, Eibe Frank, Geoffrey Holmes, Bernhard Pfahringer, Peter Reutemann, and Ian H. Witten. The WEKA Data Mining Software: An Update. *SIGKDD Explorations*, 11(1), 2009.

[31] Renjie He, Balasrinivasa Rao Sajja, Sushmita Datta, and Ponnada A. Narayana. Volume and shape in feature space on adaptive fcm in mri segmentation. *Annals of Biomedical Engineering*, 36(9):1580–1593, September 2008.

[32] K. Held et al. Markov random field segmentation of brain mr images. *IEEE Trans Med Imaging*, 16(6):878–886, 1997.

[33] K Held, E Rota Kops, B J Krause, W M Wells, R Kikinis, and H W Muller-Gartner. Markov random field segmentation of brain mr images. *Medical Imaging, IEEE Transactions on*, 16(6):878–886, 1997.

[34] Y. Hu and M. Xie. Automatic segmentation of brain ct image based on multiplicate features and decision tree. In *Proc. IEEE International Conference on Communications, Circuits and Systems*, pages 837–840, Kokura, Japan, July 2007.

[35] Xiaolei Huang, N. Paragios, and D.N. Metaxas. Shape registration in implicit spaces using information theory and free form deformations. *Pattern Analysis and Machine Intelligence, IEEE Transactions on*, 28(8):1303–1318, Aug. 2006.

[36] Langlois JA, Rutland-Brown W, and Thomas KE. Traumatic brain injury in the united states: emergency department visits, hospitalizations, and deaths. Atlanta (GA): Centers for Disease Control and Prevention, National Center for Injury Prevention and Control, 2006.

[37] Cynthia Jongen, Josien P. W. Pluim, Paul J. Nederkoorn, Max A. Viergever, and Wiro J. Niessen. Construction and evaluation of an average ct brain image for inter-subject registration. *Computers in Biology and Medicine*, 34(8):647 – 662, 2004.

[38] S. A. Kabara, M. Gabbouj, P. Dastidar, F. A. Cheikh, P. Ryymin, and E. Laasonen. Ct image texture analysis of intracerebral hemorrhage. In *Proceedings of the 2003 Finnish Signal Processing Symposium, FINSIG'03*, pages 190–194, 2003.

[39] T. Kapur, W. E. L. Grimson, W. M. Wells III, and R. Kikini. Segmentation of brain tissue from magnetic resonance images. *Medical Image Analysis*, 1(2):109–127, 1996.

[40] Michael Kass, Andrew Witkin, and Demetri Terzopoulos. Snakes: Active contour models. *International Journal of Computer Vision*, 1(4):321–331, 1988.

[41] V. S. Khoo, D. P. Dearnaley, D. J. Finnigan, A. Padhani, S. F. Tanner, and M. O. Leache. Magnetic resonance imaging (mri): considerations and applications in radiotherapy treatment planning. *Radiotherapy and Oncology*, 42(1):1–15, 1997.

[42] Nick Kingsbury. Complex wavelets for shift invariant analysis and filtering of signals. *Applied and Computational Harmonic Analysis*, 10(3):234–253, 2002.

[43] Ron Kohavi and George H. John. Wrapper for feature subset selection. *Artificial Intelligence*, 97(1-2):273–324, 1997.

[44] Pat Langley. Selection of relevant features in machine learning. In *In Proceedings of the AAAI Fall symposium on relevance*, pages 140–144. AAAI Press, 1994.

[45] LJ. Latecki, R. Lakämper, and U.Eckhardt. Shape descriptors for non-rigid shapes with a single closed contour. In *Proc. IEEE Conf. Computer Vision and Pattern Recognition*, pages 424–429, 2000.

[46] Alexandra Lauric and Sarah Frisken. Soft segmentation of ct brain data. Technical report, Technical Report TR-2007-3 Tufts University, MA, 2007.

[47] M. Lee et al. Automatic segmentation methods for various ct images using morphology operation and statistical techniques. In *Proc. IEEE International Conference on Intelligent Computer Communication and Processing*, pages 105–110, Cluj-Napoca, Romania, September 2007.

[48] Tianhu Lei and Wilfred Sewchand. Statistical approach to x-ray ct imaging and its applications in image analysis. i. statistical analysis of x-ray ct imaging. *IEEE Trans Med Imaging*, 11(1):53–61, 1992.

[49] C. K. Leung and F. K. Lam. Maximum segmented-scene spatial entropy thresholding. In *Proc. IEEE International Conference on Image Processing*, volume 3, pages 963–966, Lausanne, Switzerland, September 1996.

[50] C. K. Leung and F. K. Lam. Maximum a posteriori spatial probability segmentation. *IEE Proc-Vis. Image Signal Process.*, 144:161–167, June 1997.

[51] H. Li et al. Object recognition in brain ct-scans: Knowledge-based fusion of data. *IEEE Trans. Med. Imag.*, 14(2):212–229, 1995.

[52] Hongyi Li, R. Deklerck, B. De Cuyper, A. Hermanus, E. Nyssen, and J. Cornelis. Object recognition in brain ct-scans: knowledge-based fusion ofdata from multiple feature extractors. *Medical Imaging, IEEE Transactions on*, 14(2):212–229, 1995.

[53] Zhengrong Liang, James R. MacFall, and Donald P. Harrington. Parameter estimation and tissue segmentation from multispectral mr images. *IEEE TRANSACTIONS ON MEDICAL IMAGING*, 13(3):441–449, 1994.

[54] Chun-Chih Liao, Furen Xiao, Jau-Min Wong, and I-Jen Chiang. A simple genetic algorithm for tracing the deformed midline on a single slice of brain ct using quadratic bézier curves. In *ICDMW '06: Proceedings of the Sixth IEEE International Conference on Data Mining - Workshops*, pages 463–467, Washington, DC, USA, 2006. IEEE Computer Society.

[55] S. Lobregt and M.A. Viergever. A discrete dynamic contour model. *Medical Imaging, IEEE Transactions on*, 14(1):12–24, 1995.

[56] Sven Loncaric and Domagoj Kovacevic. A method for segmentation of ct head images. In *In Proceedings of the 9th Int'l Conference on Image Analysis and Processing*, pages 388–395, 1997.

[57] J. Maintz and M. Viergever. A survey of medical image registration. *Medical Image Analysis*, 2(1):1–36, 1998.

[58] P. Marais, R. Guillemaud, M. Sakuma, Andrew Zisserman, and Michael Brady. Visualising cerebral asymmetry. In *Proceedings of the 4th International Conference on Visualization in Biomedical Computing*, pages 411–416. Springer-Verlag, 1996.

[59] P. C. Marais, R. Guillemaud, M. Sakuma, A. Zisserman, and M. Brady. Visualising cerebral asymmetry. In *Visualization in Biomedical Computing VBC'96*, pages 411–416, Hamburg, Germany, 1996. Lecture Notes in Computer Science,K. H. Hohne and R. Kikinis, Eds, Springer.

[60] Tim Mcinerney and Demetri Terzopoulos. Topologically adaptable snakes. In *Medical Image Analysis*, pages 840–845, 1995.

[61] Tim Mcinerney and Demetri Terzopoulos. Deformable models in medical image analysis: A survey. *Medical Image Analysis*, 1:91–108, 1996.

[62] J. Meinguet. Multivariate interpolation at arbitrary points made simple. *J. Applied Math. Physics(ZAMP)*, 5:439–468, 1979.

[63] Ernest E. Moore, David V. Feliciano, and Kenneth L. Mattox. *Trauma*. McGraw-Hill Professional, 5 edition, October 2003.

[64] Hossam E. Abd El Munim and Aly A. Farag. Curve/surface representation and evolution using vector level sets with application to the shape-based segmentation problem. *IEEE Transactions on Pattern Analysis and Machine Intelligence*, 29(6):945–958, 2007.

[65] Tom Novack. Tbi inform - introduction to brain injury: Facts & stats. UAB-TBIMS, Birmingham, AL, 2000.

[66] R.A. Ochs et al. Automated classification of lung bronchovascular anatomy in ct using adaboost. *Medical Image Analysis.*, 11:315–324, 2007.

[67] S. Okie. Traumatic brain injury in the war zone. *New England Journal of Medicine*, 352:2043–2047, 2005.

[68] Michael Oren, Constantine Papageorgiou, Pawan Sinha, Edgar Osuna, and Tomaso Poggio. Pedestrian detection using wavelet templates. In *In Proc. Computer Vision and Pattern Recognition*, pages 193–199, 1997.

[69] N. Otsu. A threshold selection method from gray-level histograms. *IEEE Trans. Syst., Man, Cybern.*, 9(1):62–66, 1979.

[70] Christos H. Papadimitriou and Kenneth Steiglitz. *Combinatorial Optimization: Algorithms and Complexity*. Prentice Hall, 1982.

[71] T.N. Papas. An adaptive clustering algorithm for image segmentation. *IEEE Transactions on Signal Processing*, 40(4):901–914, 1992.

[72] Hanchuan Peng, Fuhui Long, and Chris Ding. Feature Selection Based on Mutual Information: Criteria of Max-Dependency, Max-Relevance, and Min-Redundancy. *IEEE TRANSACTIONS ON PATTERN ANALYSIS AND MACHINE INTELLIGENCE*, 27(8):1226–1238, August 2005.

[73] E. Persoon and K. Fu. Shape discrimination using fourier descriptors. *IEEE Trans. Systems, Man and Cybernetics*, 7(3):170–179, March 1977.

[74] Adrian Peter, Anand Rangarajan, and Jeffrey Ho. Shape l'$\hat{A}$ne rouge: Sliding wavelets for indexing and retrieval. In *Proc. IEEE Conf. Computer Vision and Pattern Recognition*, pages 1–8, 2008.

[75] Dzung L. Pham, Dzung L. Pham, Jerry L. Prince, and Jerry L. Prince. Adaptive fuzzy segmentation of magnetic resonance images. *IEEE Transactions on Medical Imaging*, 18:737–752, 1999.

[76] Dzung L. Pham, Chenyang Xu, and Jerry L. Prince. Current methods in medical image segmentation. *Annual Review of Biomedical Engineering*, 2:315–337, 2000.

[77] A Pitiot, H. Delingette, P.M. Thompson, and N. Ayache. Expert knowledge-guided segmentation system for brain mri. *NeuroImage*, 23(Supp. 1):S85–S96, 2004.

[78] Sylvain Prima, Sebastien Ourselin, and Nicholas Ayache. Computation of the mid-sagittal plane in 3-d brain images. *Medical Imaging, IEEE Transactions on*, 21:122–138, 2002.

[79] J. Rajapakse, J. Giedd, and J. Rapoport. Statistical approach to segmentation of single-channel cerebral mr images. *IEEE Trans. On Medical Imaging*, 16(2):176–186, 1997.

[80] W.E. Reddick, J.O. Glass, E.N. Cook, T.D. Elkin, and R.J. Deaton. Automated segmentation and classification of multispectral magnetic resonance images of brain using artificial neural networks. *Medical Imaging, IEEE Transactions on*, 16(6):911–918, Dec 1997.

[81] Marko Robnik-Sikonja and Igor Kononenko. An adaptation of relief for attribute estimation in regression. In *Proceedings of the Fourteenth International Conference on Machine Learning*, pages 296–304, 1997.

[82] R.W.Conners and C.A.Harlow. A theoretical comparison of texture algorithm. *IEEE Trans. on Pattern Analysis and Machine Intelligence*, PAMI-2(3):204–222, 1980.

[83] H. G. Schnack, H. E. Hulshoff Pol, W. F. C. Baaréaand M. A. Viergever, and R. S. Kahn. Automatic segmentation of the ventricular system from mr images of the human brain. *NeuroImage*, 14(1):95–104, July 2001.

[84] R. Schonmeyer et al. Automated segmentation of lateral ventricles from human and primate magnetic resonance images using cognition network technology. *Magnetic Resonance Imaging*, 24:1377–1387, 2006.

[85] R. Schonmeyer, D. Prvulovic, A. Rotarska-Jagiela, C. Haenschel, and D. Linden. Automated segmentation of lateral ventricles from human and primate magnetic resonance images using cognition network technology. *Magnetic Resonance Imaging*, 24(10):1377–1387, 2006.

[86] Thomas B. Sebastian, Philip N. Klein, and Benjamin B. Kimia. Recognition of shapes by editing their shock graphs. *IEEE Trans. Pattern Anal. Mach. Intell.*, 26(5):550–571, May 2004.

[87] I. W. Selesnick, R. G. Baraniuk, and N. G. Kingsbury. The dual-tree complex wavelet transform. *IEEE Signal Processing Magazine*, 22(6):123–151, 2005.

[88] D. Sharvit, J. Chan, H. Tek, and B. Kimia. Symmetry-based indexing of image databases. *J. Visual Comm. and Image Representation*, 9(4):366–380, Dec. 1998.

[89] Hasan Kamil Sucu, , FazVl Gelal, Metin Gokmen, Fqsun Demircivi Ozer, and Sevket Tektas. Can midline brain shift be used as a prognostic factor to predict postoperative restoration of consciousness in patients with chronic subdural hematoma? *Surgical Neurology*, 66:178–182, 2006.

[90] J. Talairach. *Co-Planar Stereotaxic Atlas of the Human Brain: 3-D Proportional System: An Approach to Cerebral Imaging*. Georg Thieme Verlag, 1988.

[91] Sung-Chun Tang, Sheng-Jean Huang, Jiann-Shing Jeng, and Ping-Keung Yip. Third ventricle midline shift due to spontaneous supratentorial intracerebral hemorrhage evaluated by transcranial color-coded sonography. *Journal Ultrasound Med*, 25:203–209, 2006.

[92] K. Van-Leemput. Probabilistic brain atlas encoding using bayesian inference. *Proc. MICCAI*, page 704711, 2006.

[93] Vladimir Vapnik. *The Nature of Statistical Learning Theory*. Springer, 2 edition, 1999.

[94] Fei Wang, Baba C. Vemuri, Anand Rangarajan, and Stephan J. Eisenschenk. Simultaneous nonrigid registration of multiple point sets and atlas construction. *IEEE Transactions on Pattern Analysis and Machine Intelligence*, 30(11):2011–2022, 2008.

[95] Kaiping Wei, Bin He, Tao Zhang, and Xianjun Shen. A novel method for segmentation of ct head images. *ICBBE 2007*, pages 717–720, July 2007.

[96] J. Weng, A. Singh, and M.Y. Chiu. Learning-based ventricle detection from cardiac mr and ct images. *IEEE Trans. Med. Imag.*, 16(4):378–391, 1997.

[97] J.S. Weszaka, C.R. Dyer, and A.Rosenfeld. A comparative study of texture measures for terrain classification. *IEEE Trans. on Syst., Man, Cyber.*, 1976.

[98] Wells WM, Grimson WL, Kikinis R, and Jolesz FA. Adaptive segmentation of mri data. *Medical Imaging, IEEE Transactions on*, 15(4):429–442, 1996.

[99] Jue Wu and Albert C.S. Chung. A segmentation model using compound markov random fields based on a boundary model. *Image Processing, IEEE Transactions o*, 16(1):241–252, 2007.

[100] Y. Xia, Q. Hu, A. Aziz, and W.L. Nowinski. A knowledge-driven algorithm for a rapid and automatic extraction of the human cerebral ventricular system from mr neuroimages. *NeuroImage*, 21(1):269–282, 2004.

[101] K. Xiao, S. Hock Ho, and Q. Salih. A study: Segmentation of lateral ventricles in brain mri using fuzzy c-means clustering with gaussian smoothing. *Rough Sets, Fuzzy Sets, Data Mining and Granular Computing*, 4482:161–170, 2007.

[102] Chenyang Xu, Student Member, Jerry L. Prince, and Senior Member. Snakes, shapes, and gradient vector flow. *IEEE Transactions on Image Processing*, 7:359–369, 1998.

[103] Robert T. Collins Yanxi Liu and William E. Rothfus. Robust midsagittal plane extraction from normal and pathological 3-d neuroradiology images. *Medical Imaging, IEEE Transactions on*, 20:175–192, 2001.

[104] C. Zahn and R. Roskies. Fourier descriptors for plane closed curves. *IEEE Trans. Computers*, 21(3):269–281, March 1972.

[105] Yongyue Zhang, Stephen Smith, and Michael Brady. Hidden markov random field model and segmentation of brain mr images. *IEEE Transactions on Medical Imaging*, 20:45–57, 2001.

[106] Barbara Zitová and Jan Flusser. Image registration methods: a survey. *Image and Vision Computing*, 21:977–1000, 2003.

VITA

Wenan Chen received the his B.S. in Computer Information System from Beijing Information Technology Institute in 2003. His M.S. degree is received from Computer Science of Beijing University of Technology in 2006. His research interests include biomedical signal and image processing, machine learning, computer vision and statistical data analysis.

List of Relevant Publications:

Wenan Chen, Kevin R Ward and Kayvan Najarian. Actual Midline Estimation from Brain CT Scan Using Multiple Regions Shape Matching. 20th International Conference on Pattern Recognition 2010 (ICPR 2010).

Wenan Chen, Rebecca Smith, Nooshin Nabizadeh, Charles Cockrell, Jonathan Ha, Kevin R Ward and Kayvan Najarian. Texture Analysis of Brain CT Scans for ICP Prediction. International Conference on Image and Signal Processing 2010 (ICISP 2010).

Wenan Chen, Rebecca Smith, Simina Vasilache, Kayvan Najarian, Kevin Ward, Charles Cockrell, and Jonathan Ha. "Traumatic Pelvic Injury Outcome Prediction by Extracting Features from Relevant Medical Records and X-ray Images". *IEEE International Conference on Bioinformatics and Biomedicine (IEEE BIBM 2009)*, Nov 2009.

Simina Vasilache, **Wenan Chen**, Kayvan Najarian, Kevin Ward. "Hierarchical Object Recognition in Pelvic CT Images". *31st Annual International IEEE EMBS Conference*, September, 2-6, 2009, Hilton Minneapolis, Minnesota, USA.

Wenan Chen, Rebecca Smith, Soo-Yeon Ji, Kevin R Ward and Kayvan Najarian. "Automated Ventricular Systems Segmentation in Brain CT Images by Combining Low-level Segmentation and High-level Template Matching". *BMC Medical Informatics and Decision Making*, Nov 2009, Volume 9, Suppl 1.

S.Y. Ji, **W. Chen**, K. Ward, C.A. Rickard, K. Ryan, V.A. Convertino, and K. Najarian. "Wavelet Based Analysis of Physiological Signals for Prediction of Severity of Hemorrhagic Shock". *IEEE International Conference on Complex Medical Engineering (ICME2009)*, Tempe, AZ, April 9-11, 2009.

Wenan Chen, Kayvan Najarian. "Segmentation of Ventricles in Brain CT Images Using Gaussian Mixture Model Method". *2009 IEEE/ICME International Conference on Complex Medical Engineering (ICME2009)*, April 2009.

Wenan Chen, Rebecca Smith, Soo-Yeon Ji, and Kayvan Najarian. "Automated Segmentation of Lateral Ventricles in Brain CT images". *International Workshop on Biomedical and Hearth Informatics, IEEE Conference of Bioinformatics and Biomedicine (IEEE BIBM 2008)*, Nov 2008.

Invention Disclosure:

Wenan Chen, Kevin Ward, and Kayvan Najarian, "Automated Measurement of Brain

Injury Indices Using Brain CT Images, Injury Data, and Machine Learning", *VCU Invention Disclosure*, April 2009.